5-1-2011

Robust adaptive control for a hybrid solid oxide fuel cell system

Steven Snyder

ROBUST ADAPTIVE CONTROL FOR A HYBRID SOLID OXIDE FUEL CELL SYSTEM

by

Steven Snyder

A Thesis Submitted in Partial Fulfillment of the Requirements for the Degree of Master of Science in Mechanical Engineering

Advised by

Dr. Tuhin Das, Assistant Professor, Mechanical Engineering
Department of Mechanical Engineering
Kate Gleason College of Engineering
Rochester Institute of Technology
Rochester, New York
May 2011

Approved By:

Dr. Tuhin Das,
Assistant Professor, Mechanical Engineering
Advisor _____

Dr. Agamemnon Crassidis,
Department Representative, Mechanical Engineering _____

Dr. Jason Kolodziej,
Assistant Professor, Mechanical Engineering _____

Thesis Release Permission Form

Rochester Institute of Technology

Kate Gleason College of Engineering

Robust Adaptive Control for a Hybrid Solid Oxide Fuel Cell System

I, Steven Snyder, hereby grant permission to the Wallace Memorial Library reproduce my thesis in whole or part.

Steven Snyder

Date

Acknowledgments

In many ways, I consider myself fortunate for those I had the privilege to collaborate with throughout my graduate work. I would like to acknowledge the invaluable assistance of my advisor, Dr. Tuhin Das. I am wholeheartedly thankful for his guidance, which helped me learn; his support, which helped me grow; and his encouragement, which helped me stay motivated. I would also like to thank my labmates, W. John Nowak and Sophia Su, for making the lab more than a place for work.

This work was supported in part by the Office of Naval Research under grant #N000140910272 and in part by the National Science Foundation under grant #1030744.

Abstract

Solid oxide fuel cells (SOFCs) are electrochemical energy conversion devices. They offer a number of advantages beyond those of most other fuel cells due to their high operating temperature (800-1000°C), such as internal reforming, heat as a byproduct, and faster reaction kinetics without precious metal catalysts. Mitigating fuel starvation and improving load-following capabilities of SOFC systems are conflicting control objectives. However, this can be resolved by the hybridization of the system with an energy storage device, such as an ultra-capacitor. In this thesis, a steady-state property of the SOFC is combined with an input-shaping method in order to address the issue of fuel starvation. Simultaneously, an overall adaptive system control strategy is employed to manage the energy sharing between the elements as well as to maintain the state-of-charge of the energy storage device. The adaptive control method is robust to errors in the fuel cell's fuel supply system and guarantees that the fuel cell current and ultra-capacitor state-of-charge approach their target values and remain uniformly, ultimately bounded about these target values. Parameter saturation is employed to guarantee boundedness of the parameters. The controller is validated through hardware-in-the-loop experiments as well as computer simulations.

Contents

List of Figures

Nomenclature

F	Faraday's constant = 96485.34 [coulomb/mol]
k	Anode recirculation fraction
N	Number of moles [moles]
$\mathcal{N}_{cell}$	Number of cells in series
$\dot{N}_{air}$	Molar flow rate of air [moles/sec]
$\dot{N}_f$	Molar flow rate of fuel [moles/sec]
$\dot{N}_{f,d}$	Molar flow rate demand of fuel [moles/sec]
$\dot{N}_{in}$	Anode inlet flow rate [moles/sec]
$\dot{N}_o$	Anode exit flow rate [moles/sec]
n	Number of electrons participating in electrochemical reaction [= 2]
$\mathcal{R}$	Species rate of formation [moles/sec]
R_u	Universal Gas Constant 8.314 [J/mol/K]
T	Temperature [K]
V	Volume [m^3]
$\mathcal{X}$	Mole fraction
V_{cell}	Cell voltage [V]
U	Fuel utilization [%]
U_{ss}	Steady state fuel utilization [%]
V_{fc}	Fuel cell voltage [V]
i_{fc}	Fuel cell current [A]
V_L	Load current [V]
i_L	Load current [A]
V_{uc}	Ultra-capacitor voltage [V]
i_{uc}	Ultra capacitor current [A]
$i_{uc,c}$	Ultra-capacitor current command [A]

η_1	Unidirectional dc/dc converter efficiency
η_2	Ultra-capacitor grid bi-directional dc/dc converter efficiency
β_1	$1/\eta_1$
β_2	$1/\eta_2$
β_{12}	η_1/η_2
C	Capacitance value 250 [F]
E_s	Error in ultra-capacitor state of charge
$E_{fc,t}$	Error between $i_{fc,t} - i_{fc,d}$
$E_{fc,t}$	Error between $i_{fc} - i_{fc,t}$
E_{fl}	Error between $\dot{N}_f - \dot{N}_{f,d}$
SOC	State of charge
S	State of charge of the ultra-capacitor
S_t	Target state of charge of the ultra-capacitor
$i_{fc,t}$	Fuel cell current target [A]
$i_{fc,d}$	Fuel cell current demand [A]
DC	Direct current
$\bar{\eta}_1$	Estimated unidirectional DC/DC converter efficiency
$\bar{\eta}_2$	Estimated ultra-capacitor grid bi-directional DC/DC converter efficiency
$\bar{\beta}_1$	$1/\bar{\eta}_1$
$\bar{\beta}_2$	$1/\bar{\eta}_2$
$\bar{\beta}_{12}$	Estimated ratio of η_1/η_2
e_i	Error between $\beta_i - \bar{\beta}_i$ where i is 1, 2, or 12
γ_i	Adaptation gain for $\bar{\eta}_i$ where i is 1, 2, or 12

Subscripts

a	Anode control volume
c	Cathode control volume
r	Reformer control volume

Chapter 1

Introduction

1.1 Motivation

Rising energy demands and increased environmental awareness are straining our fossil fuel-based energy infrastructure, causing prices to climb. Because of this, alternative energy sources have become an important, and very attractive, area of research [2]. One such energy technology is the fuel cell. It has a number of advantages, such as efficiency, simplicity, and low green house emissions [1]. Many fuel cell technologies have been developed over the past few decades, such as Polymer Electrolyte Membrance Fuel Cells (PEMFC), Alkaline Fuel Cells (AFC), Solid Oxide Fuel Cells (SOFC), and Molten Carbonate Fuel Cells (MCFC) [3].

One particular type of fuel cell showing significant potential is the SOFC [1]. The three main components to a fuel cell are the electrolyte, anode, and cathode. SOFCs use zirconia doped with 8-10 mole % yttria as the electrolyte. This is a solid state material with a high capability of conducting oxygen ions. The anode is typically a zirconia cermet, a mixture of a ceramic and metal. The cathode is composed of strontium-doped lanthanum manganese [1]. Mass transport of reactant and product gases must be allowed by the anode and cathode.

SOFCs operate at high temperatures (800-1000℃). This gives them advantages beyond those shared with most other fuel cells, such as internal reforming (and consequently a larger fuel flexibility), heat as a byproduct (useful for co-generation or

in a bottoming cycle), and faster reaction kinetics without precious metal (platinum) catalysts [1, 3, 4]. Moreover, the high operating temperatures provide the capability for combined heat and power (CHP) systems by using a gas turbine (GT) as a bottoming cycle to form a SOFC-GT hybrid system. Such a hybrid system can achieve system efficiencies greater than the normal limitations of GT systems [5]. However, due to their high cost and demanding safety requirements, the adoption of SOFCs has not been extensive. Most installations occur in niche applications and are heavily subsidized [6].

Like many other fuel cell technologies, SOFCs have a limited load following capability. This is because power transients result in fluctuations in the fuel utilization. Fuel utilization is defined as the ratio of hydrogen consumption by the fuel cell to the net available hydrogen in the anode inlet flow. A high utilization is needed for better efficiencies. Typically, the desired utilization is around 80 to 90% [7, 8, 9]. However, if the utilization is too high, the partial pressure of hydrogen in the fuel cell anode can reduce, causing a voltage drop and irreversible damage due to anode oxidation. This will be discussed in more detail in Chapter 2. So far, SOFC systems have been limited to uniform power applications due to this deficiency. However, recently, there has been an increasing interest in using SOFCs in mobile applications, where responsiveness is of paramount importance. In this regard, there is an intent to hybridize the fuel cell in order to circumvent one of its largest drawbacks and make use of its many advantages [10, 11], thereby making SOFCs competitive with PEM fuel cells, which have traditionally been considered for hybrid vehicle applications.

1.2 Basics of SOFCs

The Solid Oxide Fuel Cell produces electricity through electrochemical reactions. The primary reaction can be seen in Figure 1.1. Hydrogen fuel flows into the anode while

oxygen, typically from air, flows into the cathode. The electrolyte is a ceramic material that conducts only oxygen ions. The oxygen ions travel through the electrolyte to the anode where they mix with hydrogen to produce water, in the form of steam, and electrons. The electrons travel through the load and return to the cathode to ionize more oxygen. Unlike other fuel cells, the electrolyte is not a membrane that is permeable to molecules or atoms. It is strictly an ionic conductor, though only at high temperatures [12]. Hence the high operating temperatures of SOFCs.

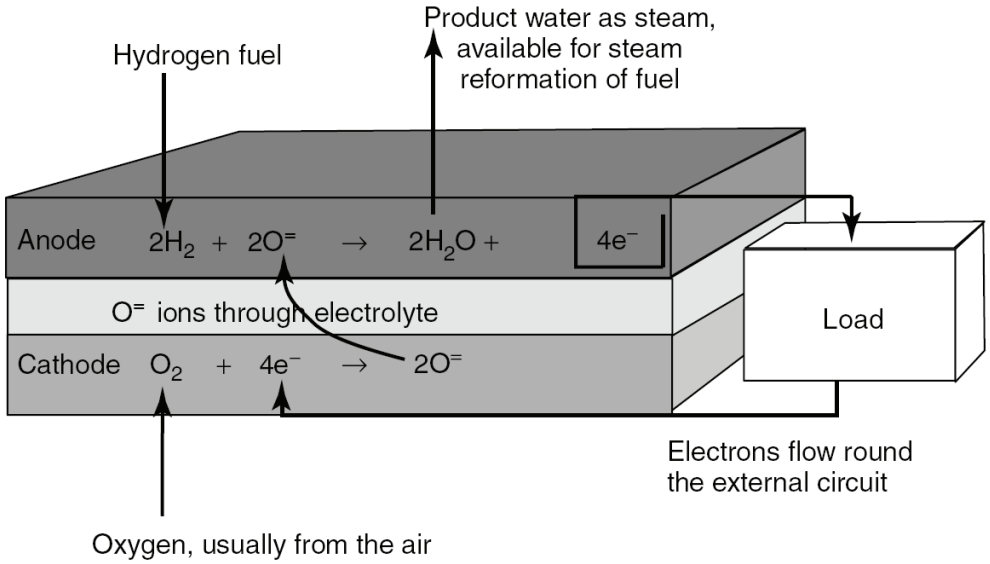

Figure 1.1: SOFC Functional Schematic [1]

While hydrogen acts as the primary fuel for producing electricity in SOFCs, it can accept other fuels as well. Because of the high operating temperatures (800 to 1000℃) and the presence of catalysts, hydrogen can be generated through internal reforming of hydrocarbon fuels within the anode chamber [1, 3]. Hydrogen can also be generated through external reforming upstream of the fuel cell stack. Some of these reforming reactions are endothermic, and, as such, require the recirculation of hot gases to provide the necessary heat to sustain these reactions [13]. Also, exothermic

reforming processes, such as POX (Partial OXidation) reforming, exist. In POX reforming, fuel is partially oxidized in order to self-sustain the reforming process.

The mathematical formulation of fuel utilization, the ratio of hydrogen consumption to the net available hydrogen in the anode of the SOFC, accounts for the available hydrogen, as well as the hydrogen that can be generated by means of internal reforming [7, 9]. Because of the SOFC's impurity tolerance, the reformer exhaust gas mixture can be sent directly to the anode with little to no purification. Though high utilization is required for high efficiency, if the utilization is too high, the partial pressure of hydrogen in the anode can be reduced, leading to voltage drop and anode oxidation, permanently damaging the fuel cell [14]. Typical target values for fuel utilization are 80-90% [7, 8, 9].

1.3 Literature Review

There are many different types of fuel cells that have been researched in the past few decades, each with its own advantages and disadvantages. Alkaline Fuel Cells (AFC) were the first fuel cells to be used in real life applications [15]. AFCs are used in space vehicles. They have a very high efficiency, and they operate at low temperatures, around 200℃. Some disadvantages of the AFC are their slow reaction kinetics, resolved by the use of porous electrodes with platinum catalysts, and their sensitivity to carbon dioxide [16]. The cost associated with the platinum catalyst and the air filtration system to remove CO_2 poses significant restriction on the use of AFCs.

Conversely, Molten Carbonate Fuel Cells (MCFC) are not poisoned by carbon dioxide [1], and are able to use it as fuel. MCFCs are classified as high-temperature fuel cells, operating temperatures around 650℃ and are thus able to internally reform CO and CO_2. According to [17], MCFCs can only reach an efficiency of about 45 to 47%. This is a major drawback for applications that require high efficiency.

Direct Methanol Fuel Cells (DMFC) are another well-known fuel cell. They use methanol as the direct fuel [18]. The benefit of this is reduced fuel storage space due to the high density of methanol. DMFC is a relatively new technology that will require significant improvement before it can feasibly be used in a larger class of applications. Currently, these cells have a very low efficiency [1].

The first modern fuel cell module to be used as a power generator was the Phosphoric Acid Fuel Cell (PAFC) [19]. With operating temperatures of 150-200℃, PAFCs are considered medium temperature fuel cells with operating temperatures around 200℃. They use a proton-conducting electrolyte and have been able to achieve efficiencies of $\approx 80\%$ in providing power and heat. However, if producing only electricity, their efficiency does not exceed 50%. The use of PAFCs has declined due to economical issues [1].

One of the most commonly known fuel cells is the Polymer Electrolyte Membrane Fuel Cell (PEMFC), also known as Proton Exchange Membrance Fuel Cells. They are used primarily in transport and non-stationary applications due to their high power density and low volume and weight [2, 6, 20, 21]. However, PEMFCs are limited by their sensitivity to impurities in the fuel source, particularly carbon monoxide, CO, and therefore require pure hydrogen to be supplied [22].

Solid Oxide Fuel Cells are high temperature fuel cells, operating around 800-1000℃. This removes the need for precious metal catalysts, reducing costs significantly. Also, the high operating temperature allows for internal reforming to occur, making SOFCs not only tolerant of carbon monoxide, but able to use it as fuel. The efficiency of SOFCs can be very high with proper utilization of fuel within the fuel cell stack. However, very high utilization can cause permanent damage to the fuel cell anode [8]. This makes controlling the utilization properly very important in order to maintain high efficiency without causing system damage. Because of these many advantages, many researchers are interested in developing methods to increase the applicability of SOFCs.

The largest difficulty in using SOFCs is their limited load following capability, which has precluded them from applications involving rapid power variations [6]. This is a common drawback to most fuel cells. It is generally attributed to the slow dynamic response of the fuel and air delivery systems, consisting of valves, pumps, and reformers [14, 23, 24, 25]. This slow response becomes evident as hydrogen or oxygen starvation, drastic voltage drop, and/or compressor surge and choke. These phenomena adversely affect the cell's durability through anode oxidation [14], and cell potential reversal, resulting in catalyst corrosion [26].

Many authors have addressed this issue by augmenting the fuel cell with an electrical storage device to create a hybrid energy system. The authors of [23] interfaced the primary, fuel cell, and secondary, ultra-capacitor, energy sources using bidirectional power electronic devices. They developed a current control strategy in order to minimize the fuel cell's voltage drop during sudden increases in the load. The control strategy is based on observing the terminal voltage of the fuel cell by controlling the ultra-capacitor currents. Simulation results show gradual prevention in any substantial drop in the fuel cell voltage as the load power increases.

In [24], current in the PEM fuel cell is rate limited in order to prevent hydrogen starvation. The strategy is based on a DC link voltage regulation that maintains the fuel cell in a steady-state condition. Once again, the fuel cell is treated as the primary power source with an ultra-capacitor as an auxiliary storage device. Power is drawn from the ultra-capacitor in such a way as to minimize mechanical stresses on the fuel cell. The ultra-capacitor current draw is synchronized with the PEMFC fuel flow and the current draw of the load.

A nonlinear reference governor approach is developed in [27] to address the problem of oxygen starvation in PEM fuel cells. Parameter uncertainties are addressed using a novel approach based on sensitivity functions. Simulation results are provided to demonstrate the controller effectiveness at incorporating robust control while solving the issue of oxygen starvation. A Model Predictive Control (MPC) approach is

developed in [25] for a fuel cell ultra-capacitor system. This controller minimizes oxygen starvation, bounds the ultra-capacitor's state-of-charge (SOC), and prevents compressor surge and choke while responding to power demands from the load. In [28], a MPC-based approach is used to improve battery performance and avoid fuel cell and battery degradation.

Other authors have proposed a wide array of controllers for hybrid fuel cell systems without specifically addressing any of the constraints mentioned above. Rule-based control strategies where the hybrid system switches between discrete operating modes are developed in [29, 30, 31]. In [29], the authors model the fuel cell ultra-capacitor hybrid vehicle power system and design a model-based controller focusing on starting conditions and the reverse regeneration of energy during braking.

In [30], the authors focus on cars powered by fuel cells with both ultra-capacitors and batteries on-board as well. They attempt to reduce hydrogen consumption while maintaining the state-of-charge of the ultra-capacitor and battery at acceptable levels. The ultra-capacitor protects the fuel cell from load transience and captures a large amount of energy from braking. For long periods of braking, or for larger power spikes, the battery is used instead. Thus the fuel consumption can be reduced significantly.

An online power management system is proposed for a hybrid fuel cell system in [31]. A multi-layered controller is discussed. The first layer controls what operating mode the system is in. The second layer employs a fuzzy logic algorithm to manage the power balance between the fuel cell and the auxiliary power module. The third, and final, layer consists of sub-controllers that set the operating point for each subsystem to reach the optimum performance.

In [32], an adaptive control strategy is used to adjust the output current of the fuel cell according to the state-of-charge of the secondary power source. A two-loop control strategy is proposed in [33] for a fuel cell ultra-capacitor hybrid system. The inner loop maintains the DC bus voltage and the outer loop regulates the fuel cell current. The authors only considered the SOFC stack operating at relative low pressure and are

concerned with the thermal dynamics in their controller design. In [34], a non-linear sliding-mode control is developed for the power management of a fuel cell system that has been hybridized with an ultra-capacitor and a battery. The ultra-capacitor module is used as an auxiliary transient power source while the battery is used for power peaks of a longer duration. The authors of [35] use local minimization of an equivalent fuel consumption variable to obtain optimal power distribution.

A differential flatness ([36]) based control strategy is developed by the authors of [37] for a fuel cell ultra-capacitor system. The fuel cell acts as the main power source with the ultra-capacitor acting as the secondary source. Two ultra-capacitors are used in this set up, a DC link capacitor and an output capacitor. The DC link capacitor connects both the primary and secondary power sources to the grid, and the output capacitor connects the load and the grid through power electronics. The fuel cell output voltage is kept constant and its dynamics are controlled.

Many of the works previously mentioned pertain to PEMFCs. Few deal with hybrid SOFC systems, and those that do take an approach focused on very specific setups or conditions. The work presented within this thesis seeks to provide a more holistic approach to handling power management in a SOFC ultra-capacitor hybrid system.

Chapter 2

Fuel Cell System

2.1 System Description

The system used in the ensuing analysis consists of a steam reformer, tubular SOFC, and combustor. Methane is used as the fuel for the system; its molar flow rate is denoted $\dot{N}_f$. Figure 2.1 contains a schematic of the overall fuel cell system. It should be noted that the control strategy, and its analysis, developed in this thesis can be extended to other system configurations and fuels.

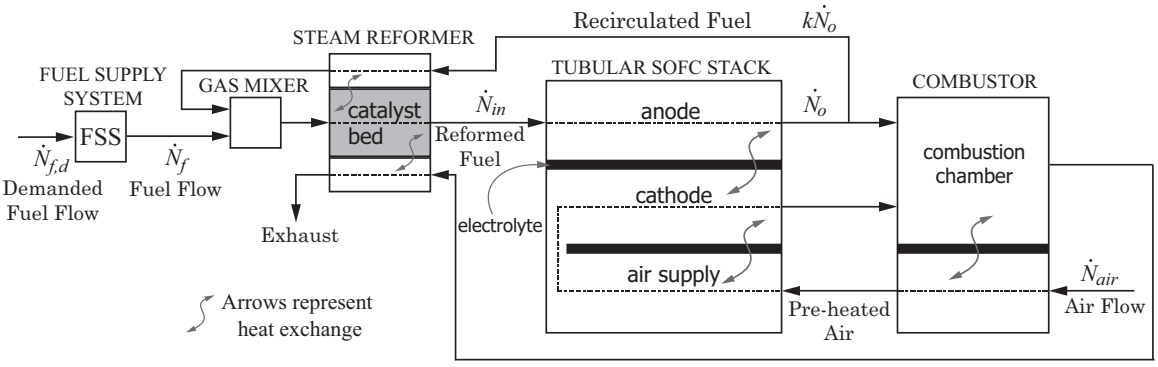

Figure 2.1: Schematic Diagram of SOFC System

The incoming fuel flow is combined with recirculated flow from the anode exhaust in the gas mixer. The product of the mixer then flows through a catalyst (nickel alumina) bed where a series of endothermic reactions reform the methane into a

hydrogen-rich gas. The reactions are summarized in Equation (2.1).

$$\begin{aligned} CH_4 + H_2O &\rightleftharpoons CO + 3H_2O \\ CO + H_2O &\rightleftharpoons CO_2 + H_2 \\ CH_4 + 2H_2O &\rightleftharpoons CO_2 + 4H_2 \end{aligned} \tag{2.1}$$

This gas is supplied to the fuel cell anode, while pre-heated air is supplied to the fuel cell cathode. The air acts as the oxygen source, and the oxygen is ionized in the cathode. The electrolyte then conducts these oxygen ions to the anode where it reacts with the hydrogen gas to form steam (H_2O) and electrons. These electrons pass through the external circuitry as the fuel cell current and return to the cathode to ionize oxygen molecules. These reactions are summarized in Equation (2.2). It should be noted that methane reforming continues in the anode as well. Figure 2.1 shows the primary electrochemical reactions of the SOFC stack.

$$\begin{aligned} \frac{1}{2}O_2 + 2e^- &\rightarrow O^{2-} \\ H_2 + O^{2-} &\rightarrow H_2O + 2e^- \end{aligned} \tag{2.2}$$

A known fraction k of the anode exhaust is recirculated, as previously mentioned. The remainder of the anode exhaust is combined with the cathode exhaust in the combustor. The combustor serves as the method of preheating the cathode air supply. The exhaust of the combustor is used to supply heat to sustain the endothermic reactions of the steam reformer.

The product of the reformer is a hydrogen-rich gas. This gas is supplied to the fuel cell anode, while pre-heated air is supplied to the fuel cell cathode. A known fraction k of the anode outlet gas is recirculated to supply heat to sustain the endothermic reactions of the steam reformer. It is then mixed with the incoming fuel flow in the gas mixer. The remaining anode outlet gas is combined with the cathode outlet gas in the combustion chamber. The combustor also serves as the method of preheating the air supply. The combustor exhaust is recirculated to supply additional heat to the steam reformer.

2.2 Fuel Utilization

A single performance parameter, fuel utilization, is usually used to quantify the performance of fuel cells. Fuel utilization, U, is defined as the ratio of hydrogen consumption to the net available hydrogen in the anode [7]. A low fuel utilization represents inefficient system operation as a lot of fuel is being wasted. However, if the fuel utilization is too high, hydrogen starvation can occur, which is unfavorable for stack integrity as it may result in voltage drop or anode oxidation [14]. In order to balance fuel efficiency and safe operation, target U values typically range between 80% and 90% [7, 8, 9]. Simulation results confirm this range for both tubular SOFCs, Figure 2.2, and planar SOFCs, Figure 2.3. Though the 80-90% range is sub-optimal, it allows for high efficiency while maintaining a sufficient buffer to provide safe operating conditions.

Fuel utilization can be expressed mathematically as

$$U = 1 - \frac{\dot{N}_O(4\mathcal{X}_{CH_4,a} + \mathcal{X}_{CO,a} + \mathcal{X}_{H_2,a})}{\dot{N}_{in}(4\mathcal{X}_{CH_4,r} + \mathcal{X}_{CO,r} + \mathcal{X}_{H_2,r})} \tag{2.3}$$

[7, 9, 14], where $\mathcal{X}$ represents the molar concentration in either the anode or reformer, as denoted by the subscripts a and r, respectively. $\dot{N}_O$ and $\dot{N}_{in}$ are shown in Figure 2.1 and represent flow rates into and out of the anode.

Figure 2.4 depicts the response of the fuel cell system to step changes in current. In this simulation, $\mathcal{N}_{cell} = 50$ and $\dot{N}_f = 7$ x 10^{-4}moles/sec, which results in a steady state utilization of $U_{ss} \approx 85\%$. As can be seen in plot (b), the current drawn from the fuel cell, i_{fc}, has a dramatic affect on the fuel utilization. Such drastic fluctuations in U shorten the life of the fuel cell due to stack damage. In the next section, an open-loop control scheme is developed based on the fuel cell's steady-state characteristics.

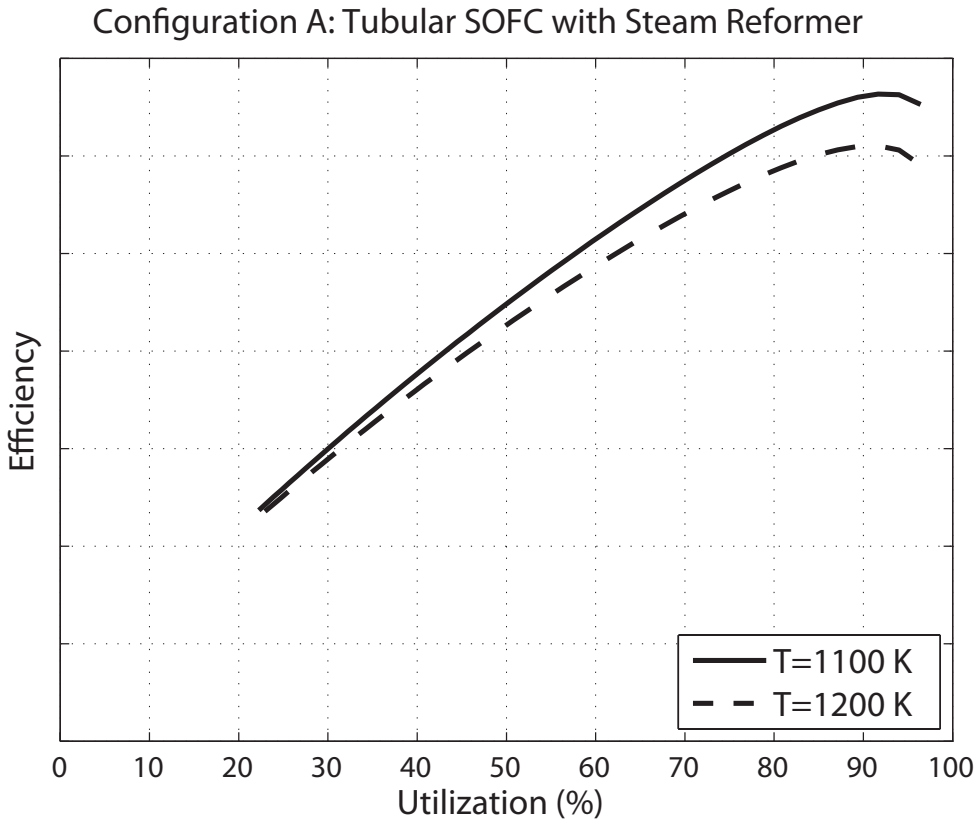

Figure 2.2: Efficiency as a Function of Utilization in a Tubular SOFC

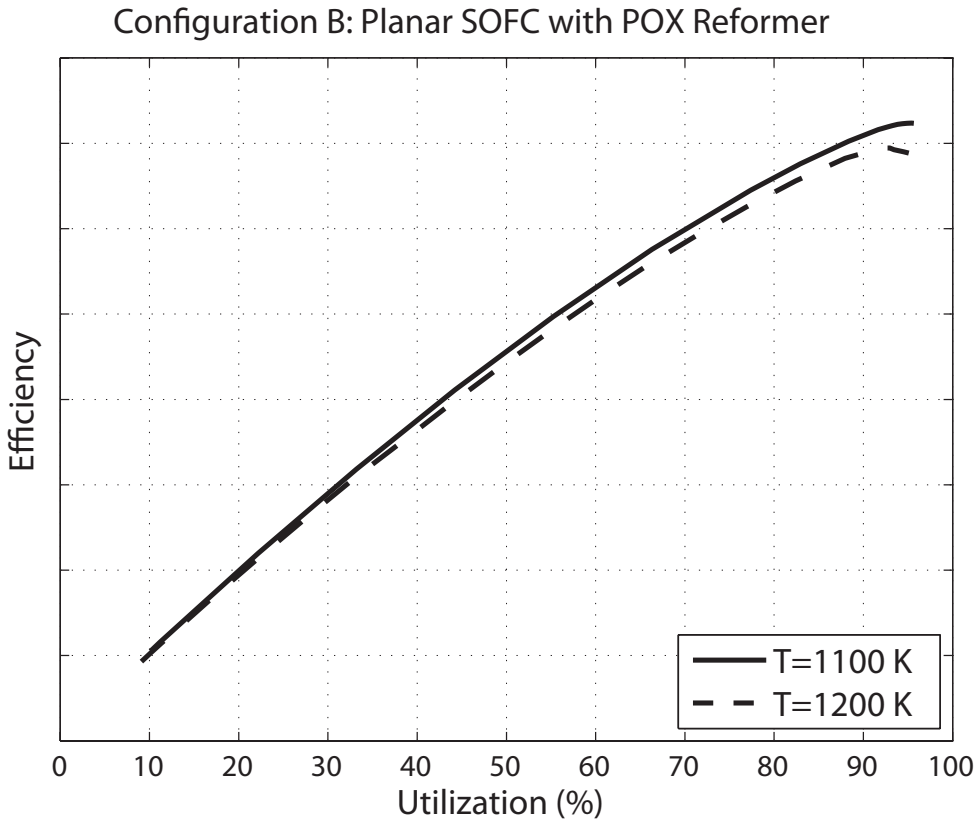

Figure 2.3: Efficiency as a Function of Utilization in a Planar SOFC

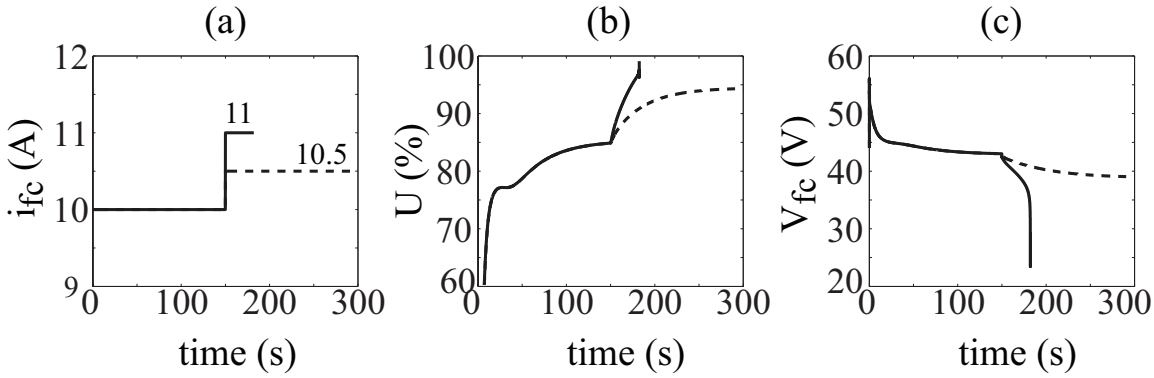

Figure 2.4: Open Loop SOFC Response to Current Draw

2.3 Open Loop Utilization Control

Using the molar balance equations (Equation (2.4) and Equation (2.5)) and the rate of electrochemical reaction equation (Equation (2.6)), the steady state utilization can be found. In these equations, N_r and N_a are the molar contents of the reformer and anode, respectively, $\mathcal{X}$ represents the molar concentration of species, subscripts a and r denote the anode and reformer, respectively, $F = 96485.34$Coul/mol is Faraday's constant, $n = 2$ is the number of electrons participating in an electrochemical reaction, and i_{fc} is the fuel cell current.

$$\begin{aligned}
\tfrac{d}{dt}(N_r\mathcal{X}_{CH_4,r}) &= k\dot{N}_o\mathcal{X}_{CH_4,a} - \dot{N}_{in}\mathcal{X}_{CH_4,r} + \mathcal{R}_{CH_4,r} + \dot{N}_f \\
\tfrac{d}{dt}(N_r\mathcal{X}_{CO,r}) &= k\dot{N}_o\mathcal{X}_{CO,a} - \dot{N}_{in}\mathcal{X}_{CO,r} + \mathcal{R}_{CO,r} \\
\tfrac{d}{dt}(N_r\mathcal{X}_{CO_2,r}) &= k\dot{N}_o\mathcal{X}_{CO_2,a} - \dot{N}_{in}\mathcal{X}_{CO_2,r} - \mathcal{R}_{CH_4,r} - \mathcal{R}_{CO,r} \\
\tfrac{d}{dt}(N_r\mathcal{X}_{H_2,r}) &= k\dot{N}_o\mathcal{X}_{H_2,a} - \dot{N}_{in}\mathcal{X}_{H_2,r} - 4\mathcal{R}_{CH_4,r} - \mathcal{R}_{CO,r} \\
\tfrac{d}{dt}(N_r\mathcal{X}_{H_2O,r}) &= k\dot{N}_o\mathcal{X}_{H_2O,a} - \dot{N}_{in}\mathcal{X}_{H_2O,r} + 2\mathcal{R}_{CH_4,r} + \mathcal{R}_{CO,r}
\end{aligned} \tag{2.4}$$

$$\begin{aligned}
\tfrac{d}{dt}(N_a\mathcal{X}_{CH_4,a}) &= k\dot{N}_{in}\mathcal{X}_{CH_4,r} - \dot{N}_o\mathcal{X}_{CH_4,a} + \mathcal{R}_{CH_4,a} \\
\tfrac{d}{dt}(N_a\mathcal{X}_{CO,a}) &= k\dot{N}_{in}\mathcal{X}_{CO,r} - \dot{N}_o\mathcal{X}_{CO,a} + \mathcal{R}_{CO,a} \\
\tfrac{d}{dt}(N_a\mathcal{X}_{CO_2,a}) &= k\dot{N}_{in}\mathcal{X}_{CO_2,r} - \dot{N}_o\mathcal{X}_{CO_2,a} - \mathcal{R}_{CH_4,a} - \mathcal{R}_{CO,a} \\
\tfrac{d}{dt}(N_a\mathcal{X}_{H_2,a}) &= k\dot{N}_{in}\mathcal{X}_{H_2,r} - \dot{N}_o\mathcal{X}_{H_2,a} - 4\mathcal{R}_{CH_4,a} - \mathcal{R}_{CO,a} - r_e \\
\tfrac{d}{dt}(N_a\mathcal{X}_{H_2O,a}) &= k\dot{N}_{in}\mathcal{X}_{H_2O,r} - \dot{N}_o\mathcal{X}_{H_2O,a} + 2\mathcal{R}_{CH_4,a} + \mathcal{R}_{CO,a} + r_e
\end{aligned} \tag{2.5}$$

$$r_e = \frac{i_{fc}\mathcal{N}_{cell}}{nF} \tag{2.6}$$

Noting that the left hand side of Equation (2.4) and Equation (2.5) are zero at steady state, the steady state utilization,

$$U_{ss} = \frac{1-k}{(4nF\dot{N}_f/i_{fc}\mathcal{N}_{cell}) - k} \tag{2.7}$$

can be found based on Equations (2.3) through (2.7). This relationship is independent of the reaction rates, flow rates, temperatures, and pressures of the fuel cell and can

thus be called an *invariant property* of the fuel cell. In addition, since k,i_{fc}, and $\dot{N}_f$ are all known or measurable, Equation (2.7) can be used as an open-loop control law to achieve a desired U_{ss} by solving for the demanded fuel flow in terms of a given current demand. This is summarized in Equation (2.8).

$$\dot{N}_{f,d} = \frac{i_{fc,d}\mathcal{N}_{cell}}{4nFU_{ss}}[1-(1-U_{ss})k] \tag{2.8}$$

While this control equation will achieve a steady-state behavior, let us examine its effectiveness to transients in the current demand.

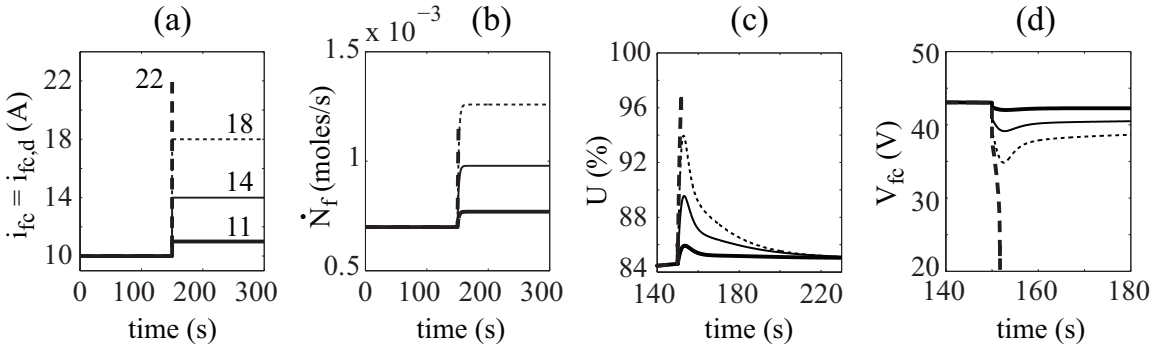

Figure 2.5: Open Loop Control Of U

Figure 2.5 shows results for multiple step changes in current demand. The system is the same as in Figure 2.4. First order dynamics are assumed for the fuel supply system with a time constant $\tau = 2sec$ and no steady-state offset. Notice that the system remains operational for a 1A step change in current demand. This is a significant improvement over the uncontrolled case. However, for larger step changes in current demand, the utilization still rises too far, causing cell damage due to hydrogen starvation and voltage drop. From the system response illustrated here, it is evident that a more sophisticated controller is required for more dynamic load transients.

2.4 Current Regulation

This section provides a brief summary of a previously developed feedback-based strategy for minimizing fluctuations in fuel utilization. For more details and further explanation, please refer to [38, 5]. While this work addresses fuel starvation, oxygen starvation is not considered as it is seldom observed in typical SOFC systems. This is because excess cathode air (air utilization $\approx$ 20 - 25 %, [39]), rather than coolants, is used for temperature control [14]. Stack temperature control *is* important, but is not considered in this work as stack temperature transients are considerably slower (order of tens of minutes) compared to transient U (order of tens of seconds) [14, 40]. Hence, this is typically addressed in a decoupled manner by manipulating the cathode air.

As seen in Figure 2.5, the actual fuel flow will not equal the demanded fuel flow during transience due to the lag introduced along the fuel path. These delays will be discussed in the following section. This inequality results in fluctuations in the utilization. To attenuate these changes in utilization, Equation (2.8) can be reversed to regulate the current draw based on the actual fuel flow, as seen in Equation (2.9).

$$i_{fc} = \frac{4nFU_{ss}\dot{N}_f}{\mathcal{N}_{cell}} \frac{1}{[1-(1-U_{ss})k]} \tag{2.9}$$

Figure 2.6 illustrates the current regulation approach. This approach assumes no knowledge of the dynamic character of the FSS, though measurement of the actual fuel flow, $\dot{N}_f$, is assumed available, and mitigates transient fluctuations in utilization in a straightforward and effective manner, as seen in Figure 2.7.

From these results, it is evident that the transience in U has been significantly reduced by the current regulation control approach. While the transience in U has been diminished (see plot (c)), it has not be completely eliminated. Still, this control strategy greatly increases the allowable current demand. One disadvantage to this strategy is that it creates a discrepancy between the demanded fuel cell current, $i_{fc,d}$ and the actual delivered current, i_{fc} during transients (see plot (a)). This disparity

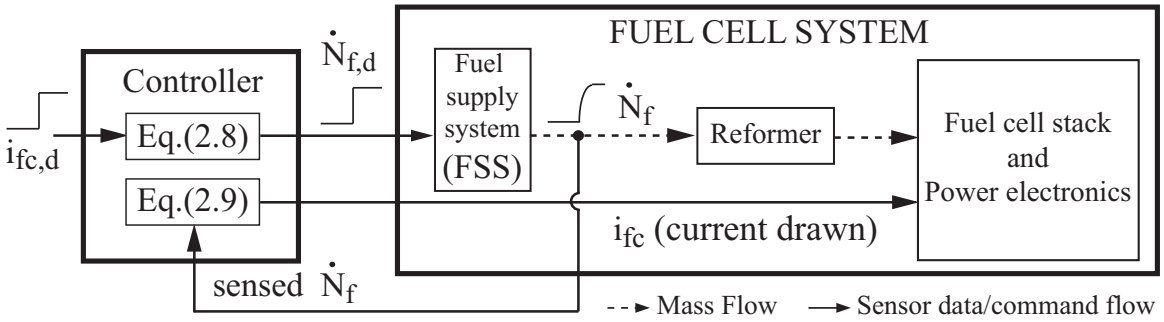

Figure 2.6: Transient Control of U through Current Regulation

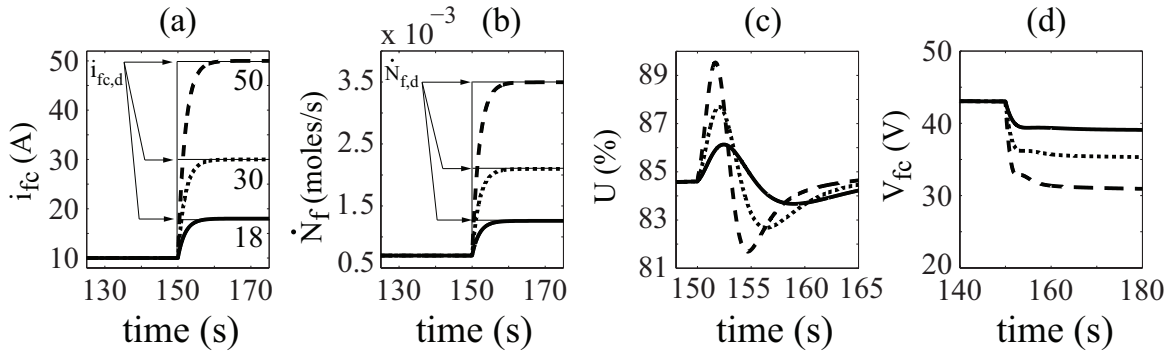

Figure 2.7: Effect of Current Regulation During Transience with First Order Dynamics

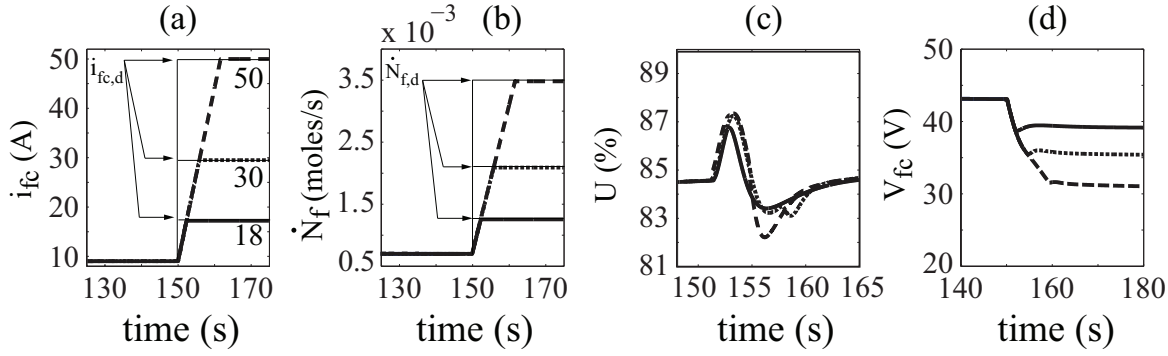

Figure 2.8: Effect of Current Regulation During Transience with Rate Limit Dynamics

can be addressed by hybridizing the fuel cell with an energy storage device, such as an ultra-capacitor. The addition of the energy storage device requires the maintenance of the device's state-of-charge (SOC) in order to prevent charge depletion or overcharge.

2.5 Lag Induced by the Fuel Path

As we saw previously, delays occurring along the fuel path cause disturbances to the utilization during transients in fuel cell current demand. This lag is primarily attributed to two sources, the fuel supply system, and the reformer, denoted D1 and D2, respectively, in Figure 2.9. The current regulation described in Section 2.4

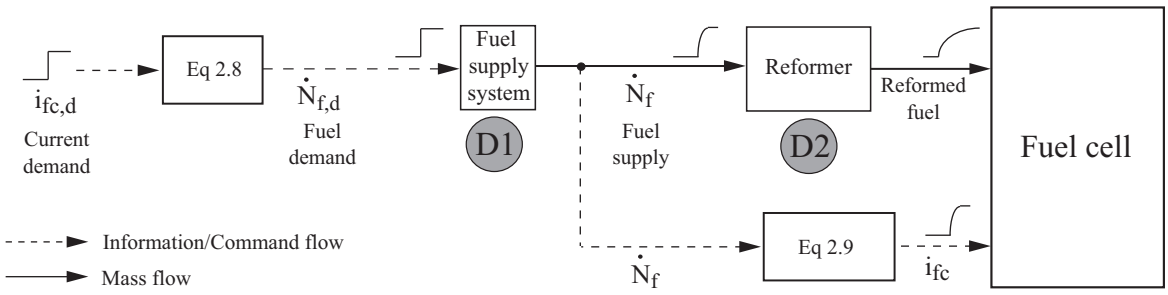

Figure 2.9: Delays Along the Fuel Path and Sensor Placement

compensates for D1. The remaining transience seen in Figure 2.7(c) and Figure 2.8(c) are attributed to D2. While previous observations regarding the fuel supply system have assumed a first order response or a ramped response, they apply to a wide range of dynamic responses.

For perfect disturbance rejection, i_{fc} must be regulated to account for D2 as well. Accomplishing this with a model-independent approach is a potential topic for future research. Typically, the effect of D1 is more pronounced than D2. However, the effect of D2 is magnified if the reformer's void volume is much larger than the anode volume or when there exist severe flow restrictions between the reformer and anode. Neither of these cases will occur during any study discussed herein.

2.6 Fuel Supply System

A model of the FSS is not required for control development of the hybrid system. However, certain assumptions as to its character are made.

1. The FSS is assumed to be a combination of components such as a fuel pump and/or valves and a controller. The closed-loop system delivers flow $\dot{N}_f$ in response to a demanded flow $\dot{N}_{f,d}$.

2. The state equation (or model) of the FSS is assumed to be unknown.

3. The delivered fuel $\dot{N}_f$ is assumed to track the reference signal $\dot{N}_{f,d}$ such that

$$|\dot{N}_f(t)| \leq \beta\left(|\dot{N}_f(t_0)|, t - t_0\right) + \gamma\left(\sup_{t_0 \leq \tau \leq t} |\dot{N}_{f,d}(\tau)|\right) \tag{2.10}$$

   where β is a class $\mathcal{KL}$ function and γ is a class $\mathcal{K}$ function. For definitions of these *comparison functions* see [41]. Equation (2.10) basically requires that $\dot{N}_f$ is eventually bounded by $\gamma\left(\sup_{t_0 \leq \tau \leq t} |\dot{N}_{f,d}(\tau)|\right)$, where the magnitude of this bound is dependent on the magnitude of $\dot{N}_{f,d}$.

The assumption that $\dot{N}_f$ meets Equation (2.10) guarantees that $\dot{N}_f$ will remain bounded for all time, resulting in a stable FSS for bounded $\dot{N}_{f,d}$. Many common system response fall into this category, including first order and ramped systems. Thus, the assumption allows us to develop a controller that is applicable to a broad class of FSS without knowing their specific structure.

Consider the first order system

$$\frac{\dot{N}_f}{\dot{N}_{f,d}}(s) = \frac{c}{\tau s + 1}$$

where c and τ are positive constants. As a function of time, we see that

$$|\dot{N}_f(t)| = |\dot{N}_f(t_0)e^{-\frac{t-t_0}{\tau}} + c\dot{N}_{f,d}(t)\left(1 - e^{-\frac{t-t_0}{\tau}}\right)|.$$

Noting that $e^{-(t-t_0)/\tau}$ is strictly positive and less than 1, it is evident that

$$|\dot{N}_f(t)| \leq |\dot{N}_f(t_0)|e^{-\frac{t-t_0}{\tau}} + c \sup_{t_0 \leq \mathcal{T} \leq t} |\dot{N}_{f,d}(\mathcal{T})|,$$

where $|\dot{N}_f(t_0)|e^{-(t-t_0)/\tau}$ is a class $\mathcal{KL}$ function $\beta\left(|\dot{N}_f(t_0)|, t-t_0\right)$, and $c\sup_{t_0\leq\mathcal{T}\leq t}|\dot{N}_{f,d}(\mathcal{T})|$ is a class $\mathcal{K}$ function $\gamma\left(\sup_{t_0\leq\mathcal{T}\leq t}|\dot{N}_{f,d}(\mathcal{T})|\right)$.

Similarly, a ramped system with $\dot{N}_f(t) = \text{sgn}(\dot{N}_{f,d} - \dot{N}_f)\alpha(t-t_0) + \dot{N}_f(t_0)$, where $\alpha > 0$, can be shown to satisfy Equation (2.10), as well. If $\dot{N}_f(t_0) \geq \dot{N}_{f,d}$, the system can be bounded by a first order response $y(t) = (y(t_0) - y_d)e^{-\lambda(t-t_0)}$, where $\lambda \leq \frac{\alpha}{y_d - y(t_0)}$, $y(t_0) = \dot{N}_f(t_0)$, and $y_d = \dot{N}_{f,d}$, such that $\dot{N}_f(t) \leq y(t)$ for all t. In this case, the functions for β and γ given above for a first order system can be applied. However, if $\dot{N}_f(t_0) < \dot{N}_{f,d}$, then $|\dot{N}_f(t)| < |\dot{N}_{f,d}|$ for all t. Therefore, the following class $\mathcal{KL}$ function β and class $\mathcal{K}$ function γ apply for all ramped FSS.

$$\beta = |\dot{N}_f(t_0)|e^{-\lambda(t-t_0)},$$

$$\gamma = \sup_{t_0\leq\mathcal{T}\leq t}|\dot{N}_{f,d}(\mathcal{T})|,$$

where a conservative λ can be calculated using extreme values of $\dot{N}_{f,d}$ and $\dot{N}_f(t_0)$. Any physical FSS will have a maximum and minimum flow rate, and $\dot{N}_{f,d}$ is bounded. Therefore, these extreme values will always exist.

Theorem 1. *If $\dot{N}_f$ satisfies Equation (2.10), then E_{fl}, defined as*

$$E_{fl} \triangleq \dot{N}_f - \dot{N}_{f,d} \tag{2.11}$$

satisfies

$$|E_{fl}(t)| \leq \beta_e(|E_{fl}(t_0)|, t-t_0) + \gamma_e\left(\sup_{t_0\leq\tau\leq t}|\dot{N}_{f,d}(\tau)|\right) \tag{2.12}$$

where β_e is a class $\mathcal{KL}$ function and γ_e is a class $\mathcal{K}$ function.

Proof. Using the triangle inequality [42] and Equation(2.11),

$$|E_{fl}(t)| \leq |\dot{N}_f(t)| + |\dot{N}_{f,d}(t)|. \tag{2.13}$$

Combining this result with Equation (2.12) results in

$$|E_{fl}(t)| \leq \beta\left(|\dot{N}_f(t_0)|, t-t_0\right) + \gamma\left(\sup_{t_0\leq\tau\leq t}|\dot{N}_{f,d}(\tau)|\right) + |\dot{N}_{f,d}(t)|. \tag{2.14}$$

Rearranging Equation (2.11) and again applying the triangle inequality produces

$$\dot{N}_f(t_0) = E_{fl}(t_0) + \dot{N}_{f,d}(t_0) \Rightarrow |\dot{N}_f(t_0)| \leq |E_{fl}(t_0)| + |\dot{N}_{f,d}(t_0)|. \tag{2.15}$$

As β is a class $\mathcal{KL}$ function, Equation (2.14) and Equation (2.15) can be combined to form

$$|E_{fl}(t)| \leq \beta\left(|E_{fl}(t_0)| + |\dot{N}_{f,d}(t_0)|, t - t_0\right) + \gamma\left(\sup_{t_0 \leq \tau \leq t} |\dot{N}_{f,d}(\tau)|\right) + |\dot{N}_{f,d}(t)|. \tag{2.16}$$

Next, note that

$$\beta\left(|E_{fl}(t_0)| + |\dot{N}_{f,d}(t_0)|, t - t_0\right) \leq \begin{cases} \beta\Big(2|E_{fl}(t_0)|, t - t_0\Big) & \text{if } |E_{fl}(t_0)| \geq |\dot{N}_{f,d}(t - t_0)| \\ \beta\left(2|\dot{N}_{f,d}(t_0)|, t - t_0\right) & \text{if } |E_{fl}(t_0)| \leq |\dot{N}_{f,d}(t - t_0)| \end{cases}$$

Thus it follows that

$$\beta\left(|E_{fl}(t_0)| + |\dot{N}_{f,d}(t_0)|, t - t_0\right) \leq \ \beta\Big(2|E_{fl}(t_0)|, t - t_0\Big) + \beta\left(2|\dot{N}_{f,d}(t_0)|, t - t_0\right).$$

Noting that a class $\mathcal{KL}$ function is decreasing with respect to the second term, $\beta\left(2|\dot{N}_{f,d}(t_0)|, t - t_0\right) \leq \beta\left(2|\dot{N}_{f,d}(t_0)|, 0\right)$. Therefore, the flow error magnitude is bounded as expressed in Equation (2.12) where

$$\beta_e = \beta\Big(2|E_{fl}(t_0)|, t - t_0\Big)$$

is a class $\mathcal{KL}$ function and

$$\gamma_e\left(\sup_{t_0 \leq \tau \leq t} |\dot{N}_{f,d}(\tau)|\right) = \beta\left(2 \sup_{t_0 \leq \tau \leq t} |\dot{N}_{f,d}(\tau)|, 0\right) + \gamma\left(\sup_{t_0 \leq \tau \leq t} |\dot{N}_{f,d}(\tau)|\right) + \sup_{t_0 \leq \tau \leq t} |\dot{N}_{f,d}(\tau)|$$

is a class $\mathcal{K}$ function. □

Since E_{fl} satisfies Equation (2.12), it is ultimately bounded by some function of $|\dot{N}_{f,d}|$. The developed control strategy for the hybrid system will be robust to this bounded error. The next section introduces the hybrid system.

Remark 1. *Consider a system with input r and output y, where $r, y \in \mathcal{R}^n$. If $y(t)$ satisfies*

$$||y(t)|| \leq \beta\left(||y(t_0)||, t - t_0\right) + \gamma\left(\sup_{t_0 \leq \tau \leq t} ||r(\tau)||\right)$$

where β is a class $\mathcal{KL}$ function and γ is a class $\mathcal{K}$ function, then the error $e(t) = y(t) - r(t)$ satisfies

$$||e(t)|| \leq \beta_e\left(||y(t_0)||, t - t_0\right) + \gamma_e\left(\sup_{t_0 \leq \tau \leq t} ||r(\tau)||\right)$$

where β_e is a class $\mathcal{KL}$ function and γ_e is a class $\mathcal{K}$ function, given by

$$\beta_e\left(||e(t_0)||, t - t_0\right) = \beta\left(2||e(t_0)||, t - t_0\right)$$

$$\gamma_e\left(\sup_{t_0 \leq \tau \leq t} ||r(\tau)||\right) = \beta\left(2 \sup_{t_0 \leq \tau \leq t} ||r(\tau)||, 0\right) + \gamma\left(\sup_{t_0 \leq \tau \leq t} ||r(\tau)||\right) + \sup_{t_0 \leq \tau \leq t} ||r(\tau)||$$

Proof. The proof is identical to that of Theorem 1. □

2.7 Hybrid System

Figure 2.10 depicts a schematic of the hybrid system. In it, the fuel cell and ultra-capacitor are connected in parallel to the load via DC/DC converters, C_1 and C_2. From this figure, it follows that the instantaneous power balance is

$$V_L i_L = \eta_1 V_{fc} i_{fc} + \eta_2 V_{uc} i_{uc}, \tag{2.17}$$

where η_1 is the efficiency of C_1, and η_2 is the efficiency of C_2. For control development and analysis, the following are assumed:

- The load voltage, V_L is held constant. This could be done by operating either C_1 or C_2 in voltage control mode, and the other in current control mode. This work uses C_1 in voltage control mode and C_2 in current control mode. Thus, C_1 regulates the fuel cell voltage while C_2 commands the ultra-capacitor current $i_{uc,c}$ (it is assumed that $i_{uc} = i_{uc,c}$).

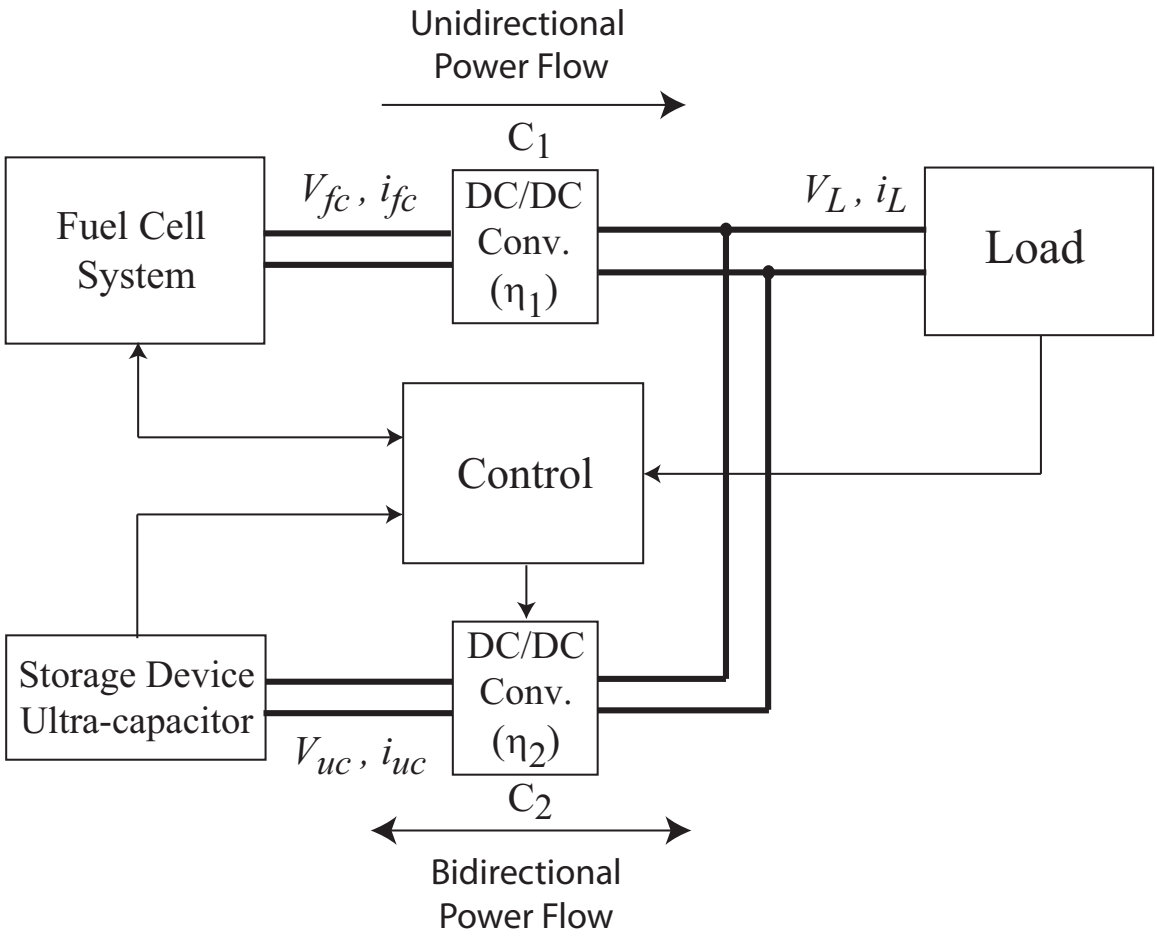

Figure 2.10: Schematic of Hybrid System

- The SOFC is operated in constant utilization mode, causing the fuel cell voltage to vary with the power draw due to the voltage-current characteristics of the fuel cell. This voltage is regulated by C_1.

- The demanded fuel flow, $\dot{N}_{f,d}$, and the ultra-capacitor current, i_{uc}, are treated as the control inputs. It should be noted that i_{uc} is commanded in both directions as C_2 is a bi-directional DC/DC converter.

- Measurements of V_{fc}, V_{uc}, i_L, i_{fc}, and $\dot{N}_f$ are available.

- The DC/DC converter efficiencies, η_1 and η_2 are unknown and time-varying, but with known bounds

$$0 \leq \eta_{1,min} \leq \eta_1(t) \leq \eta_{1,max}, \quad 0 \leq \eta_{2,min} \leq \eta_2(t) \leq \eta_{2,max}.$$

  Controller estimates for these efficiences are denoted $\bar{\eta}_1 \in [\eta_{1,min}, \eta_{1,max}]$ and $\bar{\eta}_2 \in [\eta_{2,min}, \eta_{2,max}]$.

Chapter 3

Control Design

3.1 Control Objectives

There are three primary control objectives for the hybrid system:

1. to minimize fluctuations in the fuel cell utilization
2. to maintain the SOC of the ultra-capacitor at a desired value, and
3. to meet load requirements while ensuring robustness to uncertainties in the system.

3.2 Adaptive Control

The schematic diagram shown in Figure 3.1 represents the adaptive controller for the hybrid SOFC ultra-capacitor system. The fuel cell is the primary power source while the ultra-capacitor acts as a secondary power source. The ultra-capacitor assists during periods of power transience such that large fluctuations in the fuel cell utilization are prevented. The efficiencies of the DC/DC converters that connect the power sources to the load are unknown. The adaptive controller is designed to estimate these values in suitable parametric form.

As shown in Equation (2.8), the demanded fuel flow, $\dot{N}_{f,d}$, is an algebraic function of the demanded fuel cell current, $i_{fc,d}$. As the fuel cell is the primary power source,

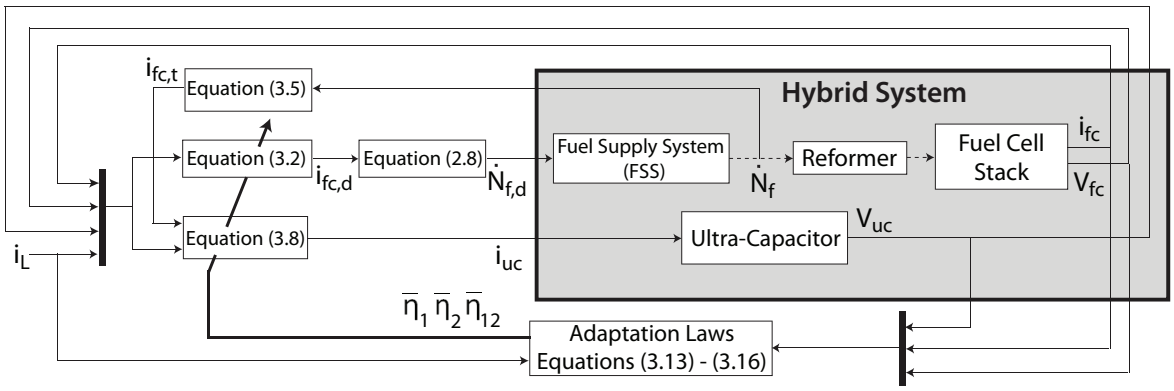

Figure 3.1: Adaptive Control Approach

the demanded fuel cell current would ideally be calculated by Equation (3.1) in order to meet the load requirements.

$$i_{fc,d} = \frac{V_L i_L}{\eta_1 V_{fc}} \tag{3.1}$$

However, as the DC/DC converter efficiency is unknown, an estimate must be used in place of the actual value. Also, during transience, the fuel cell will be incapable of meeting the load demand due to the current shaping. The power deficit will be compensated by the ultra-capacitor. This will result in a deviation of the ultra-capacitor state of charge from the target value. The state of charge must be returned to its target value based on the fuel cell current. Therefore, the demanded fuel cell current can be practically calculated by Equation (3.2) in the presence of uncertainties.

$$i_{fc,d} = \frac{V_L i_L}{\bar{\eta}_1 V_{fc}} + g(E_s) \tag{3.2}$$

The function $g(E_s)$ is used to control the ultra-capacitor state of charge in order to prevent overcharge or overdischarge. It is a function of E_s, the error between the measured state of charge, S, and the target state of charge, S_t, as expressed in Equation (3.3).

$$E_s = S - S_t \tag{3.3}$$

The target state of charge is chosen in order to allow the ultra-capacitor to act

as an energy buffer, as well as to allow it to absorb extra power during load transience. The state of charge is calculated by Equation (3.4), where the measured ultra-capacitor voltage is V_{uc}, and the maximum ultra-capacitor voltage is V_{max}.

$$S = \frac{V_{uc}}{V_{max}} \tag{3.4}$$

Since $\dot{N}_f$ is lagged by the FSS and the reformer, as discussed in Section 2.5, $\dot{N}_{f,d}$ (Equation (2.8)) is not realized. Instead, we assume the actual fuel flow is measured. Based on the measured fuel flow, $\dot{N}_f$, the target fuel cell current, $i_{fc,t}$ can be expressed as in Equation (3.5).

$$i_{fc,t} = \frac{4nFU_{ss}\dot{N}_f}{\mathcal{N}_{cell}} \frac{1}{[1-(1-U_{ss})k]} \tag{3.5}$$

However, we are not able to directly command $i_{fc,t}$ due to the hardware setup. Instead, we must calculate and command the ultra-capacitor current. Because of delays in the fuel supply system, a discrepancy exists between the target fuel cell current and the demanded fuel cell current, and consequently a power mismatch occurs between the fuel cell and load. The difference between the target fuel cell current and the demanded fuel cell current is known as $E_{fc,t}$, as shown in Equation (3.6).

$$E_{fc,t} = i_{fc,t} - i_{fc,d} \tag{3.6}$$

The ultra-capacitor must compensate for the power mismatch using Equation (3.7) to control the ultra-capacitor current, i_{uc}.

$$i_{uc} = \frac{V_L i_L - \eta_1 V_{fc} i_{fc,t}}{\eta_2 V_{uc}} \tag{3.7}$$

Once again, the efficiencies of the power converters are unknown. Therefore, estimates must be used in the actual implementation of Equation (3.7). Also, because of uncertainties, the actual fuel cell current is not necessarily going to be match the target current, $i_{fc} \neq i_{fc,t}$. Therefore, Equation (3.8) is used in place of Equation (3.7) in the presence of uncertainties.

$$i_{uc} = \frac{V_L i_L - \bar{\eta}_1 V_{fc} i_{fc,t}}{\bar{\eta}_2 V_{uc}} + h(E_{fc}) \tag{3.8}$$

The function $h(E_{fc})$ is used to account for the discrepancy between the actual, measured fuel cell current, i_{fc}, and the target fuel cell current, $i_{fc,t}$. It is based on the error between these two values, as expressed in Equation (3.9).

$$E_{fc} = i_{fc} - i_{fc,t} \tag{3.9}$$

Based on Equation (3.2) and Equation (3.8), the following parameters are identified

$$\beta_1 = \frac{1}{\eta_1}, \quad \beta_2 = \frac{1}{\eta_2}, \quad \beta_{12} = \frac{\eta_1}{\eta_2}, \tag{3.10}$$

with parameter estimates given by

$$\bar{\beta}_1 = \frac{1}{\bar{\eta}_1}, \quad \bar{\beta}_2 = \frac{1}{\bar{\eta}_2}, \quad \bar{\beta}_{12} = \frac{\bar{\eta}_1}{\bar{\eta}_2}, \tag{3.11}$$

and parameter errors represented as

$$e_1 = \beta_1 - \bar{\beta}_1, \quad e_2 = \beta_2 - \bar{\beta}_2, \quad e_{12} = \beta_{12} - \bar{\beta}_{12}. \tag{3.12}$$

The following parameter adaptation law is proposed for the system:

$$\begin{aligned} \dot{\bar{\beta}}_1 &= -\frac{V_L i_L E_s}{C V_{max} V_{uc}} \gamma_1 + g_1, \quad \gamma_1 > 0 \\ \dot{\bar{\beta}}_2 &= \frac{V_L i_L E_{fc}}{V_{uc}} \gamma_2 + g_2, \quad \gamma_2 > 0 \\ \dot{\bar{\beta}}_{12} &= -\frac{V_{fc} i_{fc} E_{fc}}{V_{uc}} \gamma_{12} + g_{12}, \quad \gamma_{12} > 0 \end{aligned} \tag{3.13}$$

where γ_1, γ_2, and γ_{12} are constant parameter adaptation gains. The terms g_1, g_2, and g_{12} are designed to maintain the boundedness of the parameter estimates as follows:

$$\begin{aligned} g_1 &= \begin{cases} -d_1 & \text{if } \bar{\beta}_1 \geq \beta_{1,max} \text{ and } d_1 > 0 \\ & \text{or } \bar{\beta}_1 \leq \beta_{1,min} \text{ and } d_1 < 0 \\ 0 & \text{otherwise} \end{cases} \\ d_1 &= -\gamma_1 V_L i_L E_s / (C V_{max} V_{uc}) \end{aligned} \tag{3.14}$$

$$\begin{aligned} g_2 &= \begin{cases} -d_2 & \text{if } \bar{\beta}_2 \geq \beta_{2,max} \text{ and } d_2 > 0 \\ & \text{or } \bar{\beta}_2 \leq \beta_{2,min} \text{ and } d_2 < 0 \\ 0 & \text{otherwise} \end{cases} \\ d_2 &= \gamma_2 V_L i_L E_{fc} / V_{uc} \end{aligned} \tag{3.15}$$

$$
\begin{aligned}
g_{12} &= \begin{cases} -d_{12} & \text{if } \bar{\beta}_{12} \geq \beta_{12,max} \text{ and } d_{12} > 0 \\ & \text{or } \bar{\beta}_{12} \leq \beta_{12,min} \text{ and } d_{12} < 0 \\ 0 & \text{otherwise} \end{cases} \\
d_{12} &= -\gamma_{12} V_{fc} i_{fc} E_{fc} / V_{uc}.
\end{aligned} \tag{3.16}
$$

Of the three objectives listed in Section 3.1, the first is handled by the current shaping method presented in Section 2.4. The second and third can be summarized as a need to stabilize the origin $(E_s, E_{fc}) = (0, 0)$ in the presence of a time varying load, i_L, via the design of $i_{fc,d}$ and i_{uc}, as expressed in Equation (3.2) and Equation (3.8), respectively. Moreover, the dynamics of the fuel supply system result in a transient error between $i_{fc,d}$ and $i_{fc,t}$, as expressed in Equation (3.6); the dynamics of which are characteristic of the fuel supply system and are considered to be unknown during the controller design. Based on certain general stability properties of the fuel supply system error variable, $E_{fl} = \dot{N}_f - \dot{N}_{f,d}$, stability of the overall hybrid system can be ensured, as proved by the following theorems.

Theorem 2. *If the origin of* $\mathrm{E_{fl}}$ *is exponentially stable, then* $\bar{\mathcal{E}} = [\mathrm{E_s\ E_{fc,t}\ E_{fc}}]^{\mathrm{T}} = 0$ *is guaranteed to be an exponentially stable equilibrium by inputs* $\mathrm{i_{fc,d}}$ *and* $\mathrm{i_{uc}}$ *expressed in Equation (3.2) and Equation (3.8), respectively, with* $\mathrm{g(E_s)}$ *and* $\mathrm{h(E_{fc})}$ *as described below in Equation (3.17) and Equation (3.18), respectively, and parameter adaptation laws Equations (3.13,3.14,3.15,3.16).*

$$
g(E_s) = -k_s E_s, \quad k_s > 0 \tag{3.17}
$$

$$
h(E_{fc}) = k_p E_{fc} + k_d \dot{E}_{fc}, \quad k_p, k_d > 0 \tag{3.18}
$$

Proof. A Fuel Supply System with exponential tracking of the $\dot{N}_{f,d}$ reference signal implies that constants $\gamma, \zeta, r_0 > 0$ exist such that the inequality expressed in Equation (3.19) holds true.

$$
|E_{fl}(t)| \leq |E_{fl}(t_0)| e^{-\zeta(t-t_0)}, \quad \forall |E_{fl}(t_0)| < r_0 \tag{3.19}
$$

Based on Equation (2.8) and Equation (2.9), as well as the error definitions, Equation (2.11) and Equation (3.6), E_{fl} can be described as an algebraic function of $E_{fc,t}$ as shown in Equation (3.20). Note that σ is a known constant.

$$E_{fl} = \sigma E_{fc,t}, \quad \sigma = \frac{\mathcal{N}_{cell}[1-(1-U_{ss})k]}{4nFU_{ss}} \tag{3.20}$$

From Equation (3.19) and Equation (3.20), it stands that exponential stability of the origin of $E_{fc,t}$ is true as well, as described in Equation (3.21).

$$|E_{fc,t}(t)| \leq |E_{fc,t}(t_0)|e^{-\zeta(t-t_0)}, \quad \forall |E_{fc,t}(t_0)| < \frac{r_0}{\sigma} \tag{3.21}$$

Equation (3.21), in conjunction with *Converse Lyapunov Theorems* [41], guarantees that there exists a positive definite and decrescent Lyapunov function, $\bar{V}_{FSS}$, that satisfies the inequalities of Equation (3.22), where $\alpha_2 > \alpha_1 > 0$, and $\alpha_3 > 0$.

$$\alpha_1 E_{fc,t}^2 \leq \bar{V}_{FSS}(E_{fc,t}) \leq \alpha_2 E_{fc,t}^2, \quad \dot{\bar{V}}_{FSS} \leq -\alpha_3 E_{fc,t}^2 \tag{3.22}$$

In order to analyze the overall hybrid system, a Lyapunov function candidate for the system is proposed in Equation (3.23).

$$\bar{V} = \frac{1}{2}\left(\frac{\eta_2}{\eta_1}E_s^2 + k_d E_{fc}^2 + \frac{e_1^2}{\gamma_1} + \frac{e_2^2}{\gamma_2} + \frac{e_{12}^2}{\gamma_{12}}\right) + \bar{V}_{FSS} \tag{3.23}$$

As can be seen in Equation (3.24), this Lyapunov candidate is both positive definite and decrescent.

$$\begin{aligned} &\min\left(\alpha_1, k_d, \frac{\eta_2}{\eta_1}, \frac{1}{\gamma_1}, \frac{1}{\gamma_2}, \frac{1}{\gamma_{12}}\right)\left(\bar{\mathcal{E}}^2 + e_1^2 + e_2^2 + e_{12}^2\right) \leq \bar{V}(x,t) \\ &\bar{V}(x,t) \leq \max\left(\alpha_2, k_d, \frac{\eta_2}{\eta_1}, \frac{1}{\gamma_1}, \frac{1}{\gamma_2}, \frac{1}{\gamma_{12}}\right)\left(\bar{\mathcal{E}}^2 + e_1^2 + e_2^2 + e_{12}^2\right) \end{aligned} \tag{3.24}$$

Differentiating the Lyapunov candidate along the state trajectories produces Equation (3.25). Note that η_1 and η_2 are not differentiated as they are treated as constant parameters in the adaptive control. In actuality, they may be slowly varying.

$$\dot{\bar{V}} = \frac{\eta_2}{\eta_1}E_s\dot{E}_s + k_d E_{fc}\dot{E}_{fc} + \frac{e_1\dot{e}_1}{\gamma_1} + \frac{e_2\dot{e}_2}{\gamma_2} + \frac{e_{12}\dot{e}_{12}}{\gamma_{12}} + \dot{\bar{V}}_{FSS} \tag{3.25}$$

The ultra-capacitor dynamics can be simply modeled by Equation (3.26), where C is the capacitance. This can be combined with Equation (3.3) to produce Equation (3.27).

$$\dot{V}_{uc} = \frac{-i_{uc}}{C} \tag{3.26}$$

$$\dot{E}_s = \frac{-i_{uc}}{CV_{max}} \tag{3.27}$$

Solving Equation (3.1) for the ultra-capacitor current, Equation (3.27) can be rewritten as in Equation (3.28).

$$\dot{E}_s = -\frac{V_L i_L - \eta_1 V_{fc} i_{fc}}{\eta_2 V_{uc} C V_{max}} \tag{3.28}$$

Based on the definitions of E_{fc} and $E_{fc,t}$ from Equation (3.9) and Equation (3.6), respectively, the fuel cell current can be expressed as in Equation (3.29).

$$i_{fc} = E_{fc} + E_{fc,t} + i_{fc,d} \tag{3.29}$$

Equation (3.30) contains the state of charge error dynamics in terms of the states, derived from Equation (3.2), Equation (3.28), and Equation (3.29).

$$\frac{\eta_2}{\eta_1}\dot{E}_s = \frac{V_{fc}(E_{fc} + E_{fc,t})}{CV_{max}V_{uc}} - \frac{V_L i_L e_1}{CV_{max}V_{uc}} - \frac{k_s E_s V_{fc}}{CV_{max}V_{uc}} \tag{3.30}$$

The fuel cell current error dynamics can be described in terms of the states by combining Equation (3.1) and Equation (3.8) with the designed function $h(E_{fc})$ expressed in Equation (3.18), as shown in Equation (3.31).

$$k_d \dot{E}_{fc} = \frac{V_L i_L e_2 - V_{fc} i_{fc} e_{12}}{V_{uc}} - \alpha E_{fc}, \quad \alpha = k_p + \frac{\bar{\eta_1} V_{fc}}{\bar{\eta_2} V_{uc}} > 0 \tag{3.31}$$

Once again, it should be noted that the parameters are treated as constants within the controller. Therefore, the parameter error derivatives are the opposite of the derivative of the parameter estimates (see Equation (3.32)).

$$\dot{e}_1 = -\dot{\hat{\beta}}_1, \quad \dot{e}_2 = -\dot{\hat{\beta}}_2, \quad , \dot{e}_{12} = -\dot{\hat{\beta}}_{12} \tag{3.32}$$

Substituting Equation (3.30), Equation (3.31), and Equation (3.32) into the derivative of the Lyapunov candidate, Equation(3.25), it can be rewritten as in Equation

(3.33), where $\bar{Q}$ is defined in Equation (3.34).

$$\dot{\bar{V}} \leq \bar{\mathcal{E}}^T \bar{Q} \bar{\mathcal{E}} - \frac{e_1 g_1}{\gamma_1} - \frac{e_2 g_2}{\gamma_2} - \frac{e_{12} g_{12}}{\gamma_{12}} \tag{3.33}$$

$$\bar{Q} = \begin{bmatrix} k_s m & -\frac{m}{2} & -\frac{m}{2} \\ -\frac{m}{2} & \alpha & 0 \\ -\frac{m}{2} & 0 & \alpha_3 \end{bmatrix}, \quad m = \frac{V_{fc}}{C V_{max} V_{uc}} > 0 \tag{3.34}$$

Here, it should be noted that $\bar{Q}$ can be guaranteed to be positive definite by proper selection of the design parameters k_p and k_s. This is because C and V_{max} are constants, and $V_{fc}, V_{uc} > 0$ are bounded based on the range of operating conditions. Also, $e_i g_i$ is strictly non-negative, as defined in Equations (3.13,3.14,3.15,3.16). Therefore, using the *Rayleigh Ritz Inequality* [41], $\dot{\bar{V}}$ can be shown to be negative semi-definite as seen in Equation (3.35). From *Theorem 8.4* of [41], Equation (3.36) follows.

$$\dot{\bar{V}} \leq -\bar{\mathcal{E}}^T \bar{Q} \bar{\mathcal{E}} \leq -\inf(\lambda_{\bar{Q}}) ||\bar{\mathcal{E}}||^2 \tag{3.35}$$

$$\bar{\mathcal{E}} \to 0 \text{ as } t \to \infty \tag{3.36}$$

□

Next, we relax the conditions on the E_{fl}. This guarantees stability for a much larger class of FSS. However, due to the limited knowledge of the fuel supply dynamics in this case, the following theorem only guarantees boundedness for the state errors and cannot guarantee convergence to zero.

Theorem 3. *If* $\dot{\mathrm{N}}_{\mathrm{f}}$ *meets the conditions of Equation (2.10), allowing the application of Theorem 1,* $\mathcal{E} = [\mathrm{E_s}\ \mathrm{E_{fc}}]^{\mathrm{T}}$ *is uniformly ultimately bounded under the control given in Figure 3.1 with* $\mathrm{i_{fc,d}}$ *and* $\mathrm{i_{uc}}$ *designed as in Equation (3.2) and Equation (3.8), respectively, and with parameter adaptation laws, Equations (3.13,3.14,3.15,3.16).*

Proof. First we define a Lyapunov candidate function as

$$\bar{V} = \frac{1}{2}\left(\frac{\eta_2}{\eta_1}E_s^2 + k_d E_{fc}^2 + \frac{e_1^2}{\gamma_1} + \frac{e_2^2}{\gamma_2} + \frac{e_{12}^2}{\gamma_{12}}\right). \tag{3.37}$$

Differentiating along the system trajectories, and substituting Equation (3.30) and Equation (3.31), along with the parameter adaptation laws, Equations (3.13,3.14,3.15,3.16), results in

$$\dot{\bar{V}} \leq -\mathcal{E}^T Q \mathcal{E} + m E_s E_{fc,t} - \frac{e_1 g_1}{\gamma_1} - \frac{e_2 g_2}{\gamma_2} - \frac{e_{12} g_{12}}{\gamma_{12}}, \tag{3.38}$$

where

$$Q = \begin{bmatrix} k_s m & -\frac{m}{2} \\ -\frac{m}{2} & \alpha \end{bmatrix}, \quad m = \frac{V_{fc}}{C V_{max} V_{uc}} > 0. \tag{3.39}$$

As stated previously, the product $e_i g_i$ is strictly non-negative. Therefore, applying the *Rayleigh Ritz Inequality* and Equation (3.20), Equation (3.38) can be expressed as follows:

$$\begin{aligned}
\dot{\bar{V}} &\leq -\mathcal{E}^T Q \mathcal{E} + m E_s E_{fc,t} \\
&\leq -\inf(\lambda_{min,Q})||\mathcal{E}||^2 + m||\mathcal{E}||\,|E_{fc,t}| \\
&\leq -\inf(\lambda_{min,Q})(1-\theta)||\mathcal{E}||^2 + ||\mathcal{E}||\left(m|E_{fc,t}| - \theta\inf(\lambda_{min,Q})||\mathcal{E}||\right), \quad 0<\theta<1 \\
&\leq -\inf(\lambda_{min,Q})(1-\theta)||\mathcal{E}||^2 < 0 \qquad \forall\, ||\mathcal{E}|| > \frac{m}{\theta\inf(\lambda_{min,Q})}|E_{fc,t}| \\
&\leq -\inf(\lambda_{min,Q})(1-\theta)||\mathcal{E}||^2 < 0 \qquad \forall\, ||\mathcal{E}|| > \frac{m\sigma}{\theta\inf(\lambda_{min,Q})}|E_{fl}|
\end{aligned} \tag{3.40}$$

Now that we have proved the existence of a bound for the state vector, $\mathcal{E}$, we attempt to determine a value for the bound. Let δ_{max} be defined such that

$$\dot{\bar{V}} \leq -\inf(\lambda_{min,Q})(1-\theta)\delta_{max}^2 < 0 \quad \forall\, ||\mathcal{E}|| > \delta_{max} = \sup\left(\frac{m\sigma|E_{fl}|}{\theta\inf(\lambda_{min,Q})}\right) \quad \forall\, t \geq t_0 \tag{3.41}$$

Next, noting that $i_{fc,t}$ and $i_{fc,d}$ are strictly non-negative, and using properties of class $\mathcal{KL}$ and class $\mathcal{K}$ functions, the definition of $E_{fc,t}$ in Equation (3.6), and the

relationship between $E_{fc,t}$ and E_{fl} in Equation (3.20) allows

$$\begin{aligned} |E_{fc,t}| &\leq \sigma[\beta_e\left(|E_{fc,t}(t_0)|, 0\right) + \gamma_e\left(\sup|i_{fc,d}|\right)] \\ &\leq \sigma[\beta_e\left(|i_{fc,t}(t_0)|, 0\right) + \gamma_e\left(\sup|i_{fc,d}|\right)] \\ &\leq \sigma[\beta_e\left(\sup(i_{fc,t}), 0\right) + \gamma_e\left(\sup(i_{fc,d})\right)]. \end{aligned} \tag{3.42}$$

From Equation (3.5) and Equation (3.2),

$$\begin{aligned} \sup(i_{fc,t}) &= \frac{4nFU_{ss}\dot{N}_{f,max}}{\mathcal{N}_{cell}} \frac{1}{[1-(1-U_{ss})k]}, \\ \sup(i_{fc,d}) &= \bar{\beta}_{1,max}\frac{V_L i_{L,max}}{V_{fc,min}} + k_s S_t, \end{aligned} \tag{3.43}$$

where the limiting values can be determined from the practical range of operation of various components in the system. Combining Equation (3.41) and Equation (3.43), results in

$$\delta_{max} = \left(\frac{\sigma V_{fc,max}}{CV_{max}V_{uc,min}\theta\inf(\lambda_{min,Q})}\right)[\beta_e(\sup(i_{fc,t}), 0) + \gamma_e(\sup(i_{fc,d}))], \tag{3.44}$$

which along with Equation (3.43), shows the existence of a δ_{max} for finite system operating conditions. Now, it can be shown that the trajectories of $\mathcal{E}$ converge to the region $||\mathcal{E}|| < \delta_{max}$ in finite time. Let $\bar{V}(t_0)$ be finite, and let $||\mathcal{E}(t_0)|| > \delta_{max}$, and at time t, $||\mathcal{E}(t)|| = \delta_{max}$. Then, by applying the *Comparison Principle* [41] to Equation (3.41), we have

$$\bar{V}(t) \leq \bar{V}(t_0) - (t-t_0)\inf(\lambda_{min,Q})(1-\theta)\delta_{max}^2. \tag{3.45}$$

Recall from Equation (3.37) that, for all $t \geq t_0$,

$$\bar{V} \geq \frac{1}{2}\min\left(\frac{\eta_2}{\eta_1}, k_d\right)||\mathcal{E}||^2 \Rightarrow \bar{V} \geq \frac{1}{2}\min\left(\frac{\eta_2}{\eta_1}, k_d\right)\delta_{max}^2, \tag{3.46}$$

and therefore,

$$\Delta t = t - t_0 \leq \frac{[\bar{V}(t_0) - \frac{1}{2}\min\left(\frac{\eta_2}{\eta_1}, k_d\right)\delta_{max}^2]}{\inf(\lambda_{min,Q})(1-\theta)\delta_{max}^2}, \tag{3.47}$$

which represents a finite time interval for finite intial conditions. Additionally, because of the parameter adaptation law design, the parameter estimates are bounded,

$\beta_{i,min} \leq \beta_i \leq \beta_{i,max}$. As δ_{max} and Δt are independent of t_0, the adaptive control design proposed in Figure 3.1 ensures that $||\mathcal{E}||$ is uniformly ultimately bounded with an ultimate bound of δ_{max} and that the parameter estimates remain bounded in the presence of a FSS system meeting the conditions of Equation (2.10). □

Chapter 4

Observations

4.1 Convergence of E_{fc}

In Theorem 3, $\mathcal{E}$ is shown to be ultimately bounded. In order to obtain the target U_{ss}, E_{fc} must converge to zero. This is guaranteed by the controller designed in Chapter 3, and can be proved by Lyapunov analysis. Notice that the system consisting of the state E_{fc} and the adaptation laws for $\bar{\beta}_2$ and $\bar{\beta}_{12}$, Equations (3.13), (3.15), (3.16), (3.31), and (3.32), is independent of the state E_s, the parameter estimate $\bar{\beta}_1$, and $E_{fc,t}$. The following corollary is proven using a Lyapunov analysis of this reduced system.

Corollary 1. *For the hybrid SOFC system in Figure 2.10, the control strategy depicted in Figure 3.1 with* $\mathrm{i_{uc}}$ *designed as in Equation 3.8 with* $\mathrm{h(E_{fc}) = k_p E_{fc} + k_d \dot{E}_{fc}}$ *and parameter adaptation laws given in Equations (3.13), (3.15), and (3.16), results in* $E_{fc} \to 0$ *as* $t \to \infty$.

Proof. For the system described above, consider the following positive definite and decrescent Lyapunov function candidate, $\bar{V}$

$$\frac{1}{2}\min\left(k_d, \frac{1}{\gamma_2}, \frac{1}{\gamma_{12}}\right)||\bar{E}||^2 \leq \bar{V} = \frac{k_d E_{fc}^2}{2} + \frac{e_2^2}{2\gamma_2} + \frac{e_{12}^2}{2\gamma_{12}} \leq \frac{1}{2}\max\left(k_d, \frac{1}{\gamma_2}, \frac{1}{\gamma_{12}}\right)||\bar{E}||^2 \tag{4.1}$$

where $\bar{E} = [E_{fc}\ e_2\ e_{12}]^T$. Differentiating Equation (4.1) along system trajectories

results in

$$\dot{V} \leq -\alpha E_{fc}^2 \leq 0. \tag{4.2}$$

By applying Theorem 8.4 of [41], it can be concluded that $\lim_{t\to\infty} E_{fc}(t) = 0$. □

Corollary 1 implies that the ultimate bound, δ_{max}, on $\mathcal{E}$, found in Theorem 3, is also the ultimate bound on E_s. If we substitute the expressions for e_2 and e_{12} from Equations (3.12) and (3.13) into Equation (3.31), and we assume that the parameter estimates are not saturated, we can see in Equation (4.3) that the adaptation laws have provided integral control to the E_{fc} dynamics.

$$\begin{aligned} k_d \dot{E}_{fc} = &- \frac{\gamma_2 V_L i_L}{V_{uc}} \int_{t_0}^{t} \frac{V_L i_L E_{fc}}{V_{uc}} dt - \frac{\gamma_{12} V_{fc} i_{fc}}{V_{uc}} \int_{t_0}^{t} \frac{V_{fc} i_{fc} E_{fc}}{V_{uc}} dt \\ &- \alpha E_{fc} + \frac{V_L i_L e_2(t_0) - V_{fc} i_{fc} e_{12}(t_0)}{V_{uc}}, \quad \alpha > 0 \end{aligned} \tag{4.3}$$

The addition of this integral action guarantees the convergence of $E_{fc} \to 0$ and provides robustness against parameter uncertainties. Note that the derivative control term, $k_d E_{fc}$, is not necessary for the convergence of E_{fc}. It is simply useful in performing the stability analysis. As in all practical applications, the magnitude of k_d must be small enough in order to avoid amplification of sensor noise. If k_d is sufficiently small, the system comprising Equation (3.31) and the dynamics of e_2 and e_{12} given in Equation (3.13), would be *singularly perturbed* [41]. A singular perturbation model of a dynamical system is a state model where the derivatives of some of the states are multiplied by a small positive parameter. Due to the small parameter (k_d in this case), the system operates on two time scales. For the E_{fc}-e_2-e_{12} system described above, the fast time scale corresponds to that of E_{fc}, while the slow time scale corresponds to that of e_2 and e_{12}. The system trajectories will rapidly converge to the manifold

$$E_{fc} = \frac{V_L i_L e_2 - V_{fc} i_{fc} e_{12}}{\alpha V_{uc}},$$

with the convergence of $E_{fc} \to 0$ occurring simultaneously, yet on a larger time scale. It should be noted that application of the saturation limits in the adaptation law will

not affect the convergence of E_{fc}. They will simply restrict movement in the e_2-e_{12} plane of the state-space.

Without adaptation, the controller would yield a non-zero, steady-state E_{fc}, resulting in U_{ss} deviating from the target U_{ss} value. E_{fc} would still rapidly converge to

$$E_{fc} = \frac{V_L i_L e_2 - V_{fc} i_{fc} e_{12}}{\alpha V_{uc}},$$

however, as there are no longer any dynamics for e_2 or e_{12}, this quantity can only be minimized by increasing α. Raising the value of α requires increasing the value of k_p. Larger values of i_L will require larger values of k_p in order to keep a low $|E_{fc}|$ and to maintain U_{ss} close to its target value. As in all PID systems, if the value of k_p is too large, unmodeled dynamics and/or sensor noises can be amplified, destabilizing the system. This limits the performance of the system without adaptation.

4.2 Parameter Convergence

The development of the adaptive control resulted in three parameters, β_1, β_2, and β_{12}. However, there are only two system efficiencies involved. β_{12} is a nonlinear combination of these efficiencies and is estimated independently. Parameter convergence cannot be generally guaranteed mainly because there are three parameters, but only two dynamic equations are considered (for E_s and E_{fc}). Correct estimation of these parameters is not of particular importance for this study. Should the conditions of Theorem 2 be met, resulting in $\lim_{t\to\infty} ||\mathcal{E}|| = 0$, then, from Equation (3.30), $e_1 \to 0$, and, from Equation (3.31), $(V_L i_L e_2 - V_{fc} i_{fc} e_{12}) \to 0$ as $t \to \infty$, implying correct estimation of β_1. Moreover, if i_L is *persistently exciting* (see [41] and references within), correct estimation of β_2 and β_{12} is possible.

Figure 4.1 shows the parameter estimates from a simulation. The simulation used a pulsed load profile with pulses from 10A to 20A with a period of 250s. There is no control during the period of time prior to $t = 250$ sec. This allows for system start-up

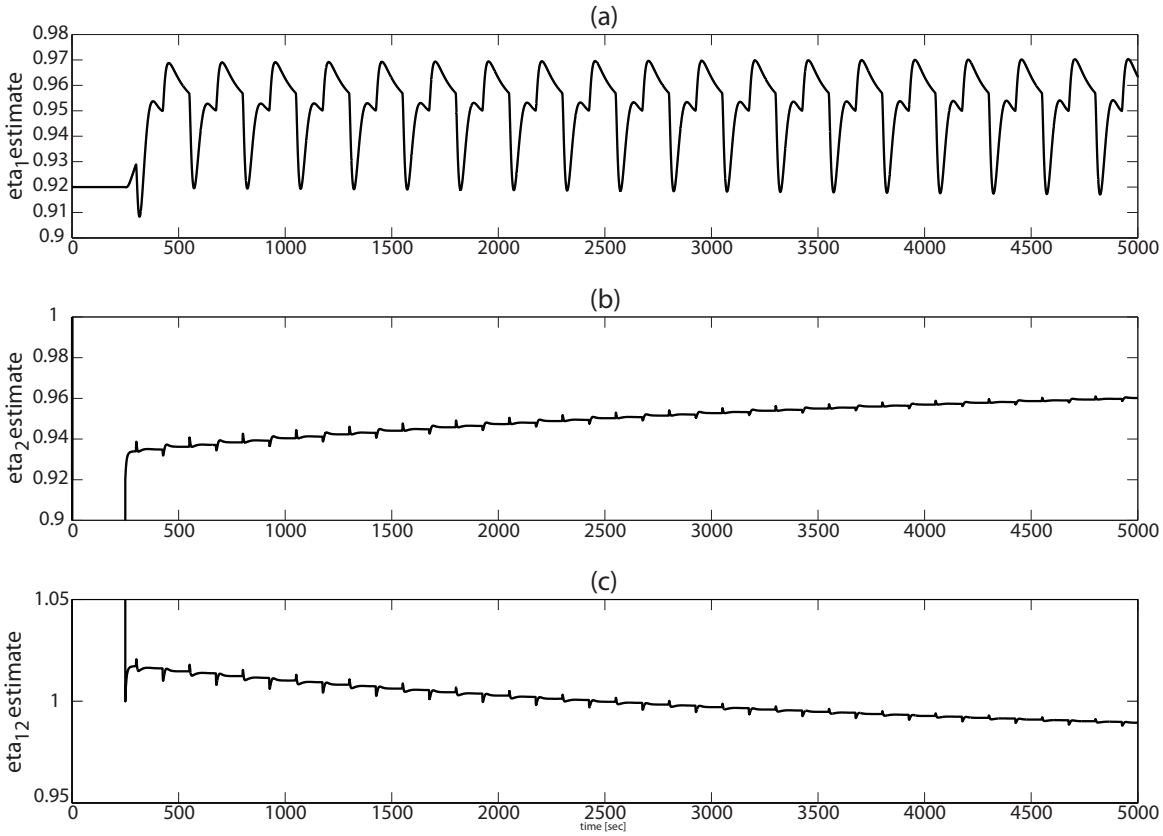

Figure 4.1: Simulation Results Suggesting Parameter Convergence

where the fuel utilization grows to its target value of 80%. The pulsed load profile does not begin until $t = 300$ sec. The efficiency values for c_1 and c_2 were 0.95 and 0.97, respectively. This results in a true value for η_1/η_2 of 0.979. Notice in plot (a) that $\bar{\eta}_1$ reaches the true value. It deviates from this value due to load changes, but converges once again towards it. Sufficient tuning could reduce the estimate's sensitivity to load changes. In plots (b) and (c), the estimate trends suggest convergence toward their true values. However, likely due to the low frequency of the load pulses, the convergence occurs slowly.

4.3 Reversal of c_1 and c_2

While all of the previous results considered a system with c_1 operating in voltage control mode and c_2 operating in current control mode, let us now consider the same system, but with c_1 and c_2 reversed, i.e. c_1 operating in current control mode, and c_2 operating in voltage control mode. This significantly simplifies the system. Since $i_{fc,t}$ can now be directly commanded, $E_{fc} = 0$. This reduces the system to a single state, E_s, a single input, $i_{fc,d}$, and a single parameter, β_1. The previous stability results are still applicable and are summarized in the following corollaries. The proofs have been omitted for conciseness, but they follow the form of the proofs of Theorem 2 and Theorem 3.

Corollary 2. *If the origin of* $\mathrm{E_{fl}}$ *is exponentially stable, the system depicted in Figure 2.10 with* c_1 *operating in current control mode and* c_2 *operating in voltage control mode is exponentially stable with input* $\mathrm{i_{fc,d}}$ *expressed in Equation (3.2),* $\mathrm{g(E_s)}$ *expressed in Equation (3.17), and parameter adaptation laws Equations (3.13, 3.14)*

If the conditions of Corollary 2 are met, note that $e_1 \to 0$, implying correct estimation of the efficiency of c_1.

Corollary 3. *If* $\mathrm{\dot{N}_f}$ *meets the conditions of Equation (2.10), allowing the application of Theoremj 1, then* $\mathrm{E_s}$ *in the system depicted in Figure 2.10 with* c_1 *operating in*

current control mode and c_2 *operating in voltage control mode is uniformly ultimately bounded under the control given in Figure 3.1 with* $\mathrm{i}_{\mathrm{fc,d}}$ *designed as in Equation (3.2) and with parameter adaptation laws, Equations (3.13,3.14).*

Chapter 5

Experimental Results

5.1 Experimental Test Stand

The hardware-in-the-loop system used for the generation of these results was developed in prior work, [43]. The system, shown in Figure 5.1, implements the hybrid system depicted schematically in Figure 2.10. The SOFC system is emulated by executing a detailed mathematical model on a dSPACE® DS1103 real time processor in conjunction with a 100V/50A programmable power supply. The power supply operates in voltage control mode with isolated analog input from the DS1103PPC controller. A DC electronic load is used to consume power and can draw a maximum power of 1.8kW with a maximum voltage of 60V and a maximum current of 120A. A unidirectional DC/DC converter, C_1, connects the emulated fuel cell to the load. The load voltage is maintained at $V_L = 24$V by C_1, which has a maximum current rating of approximately 33A. The energy storage device used is a 16V series BMOD0250-E016 ultra-capacitor from MAXWELL Technologies with $V_{max} = 16.2V$, $C = 250F$, and an internal resistance of $\approx 4.1\text{m}\Omega$. A bidirectional DC/DC converter, C_2, connects the ultra-capacitor in parallel with the emulated fuel cell to the load. It operates in current control mode and is used to command the ultra-capacitor current, i_{uc}, through analog input. The ultra-capacitor voltage is measured using voltage probes with high input impedance. Measurements for i_L and i_{fc} are obtained using two Fluke 80i-110s AC/DC durrent probes.

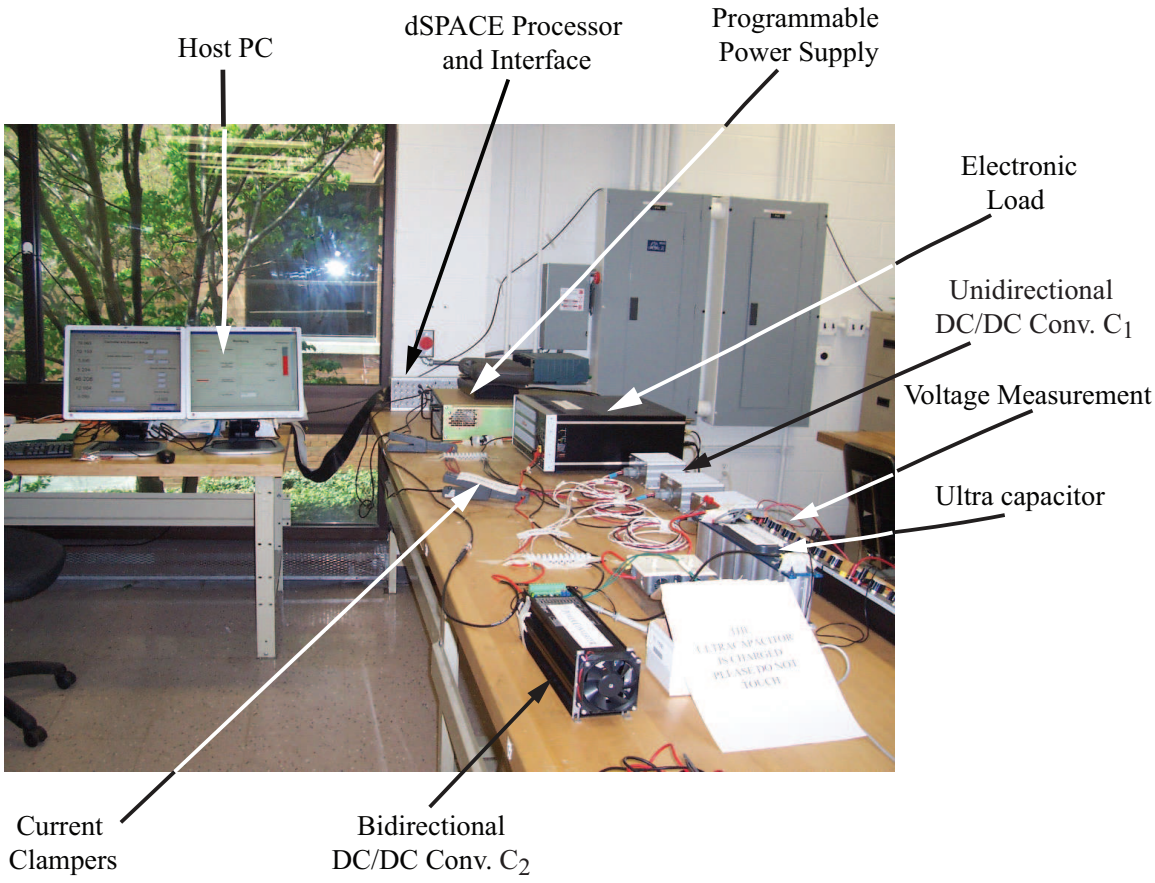

Figure 5.1: Experimental Hardware-in-the-Loop Test Stand Setup

5.2 Adaptive Control

This section contains the results of running the adaptive controller on the experimental system described in Section 5.1. The following control parameter values were used: $k_p = 0.2$, $k_d = 4 \times 10^{-5}$, $k_s = 70$, $\gamma_1 = 40$, $\gamma_2 = \gamma_{12} = 0.001$. The efficiency ranges were assumed as follows: $\eta_{1,min} = \eta_{2,min} = 0.6$ and $\eta_{1,max} = \eta_{2,max} = 1$, with initial efficiency estimates of $\bar{\eta}_1 = \bar{\eta}_2 = 0.92$. Target values for steady-state utilization and SoC were $U_{ss} = 80\%$ and $S_t = 0.80$, respectively. The fuel cell model implements an SOFC system with 50 cells connected in series, each with an area of 251cm^2. The FSS was modeled as a first order transfer function with a time constant of 2 sec.

$$\frac{\dot{N}_f(s)}{\dot{N}_{f,d}(s)} = \frac{1}{2s+1}$$

During control development, the model was assumed unknown. This FSS satisfies Equation (2.10) with

$$\beta\left(|\dot{N}_f(t_0), t-t_0\right) = e^{-0.5(t-t_0)}|\dot{N}_f(t_0)|, \quad \gamma\left(\sup_{t_0\le\tau\le t}|\dot{N}_{f,d}(\tau)|\right) = \sup_{t_0\le\tau\le t}|\dot{N}_{f,d}(\tau)|.$$

By application of Theorem 1, we can conclude that $|E_{fl}(t)|$ satisfies Equation (2.12) with functions β_e and γ_e given in Section 2.6. The conditions of Theorem 3 are met, and the controller design proposed within this theorem is applied. Figure 5.2 summarizes the results. It should be noted that, in all results in this section, the time zero represents an arbitrary time and does not relate to when the experiment was started, which is earlier than the initial time plotted. Plot (a) shows the load profile used. It consists of a series of pulses from 10A to 20A with a period of 240s. Plots (b), (c), (d), and (e) contain the variables relating to the fuel cell, i_{fc}, V_{fc}, U, and $\dot{N}_f$, respectively. The results show tight control of U despite large, instantaneous changes in i_L. The variables S and i_{uc} are shown in plots (f) and (g), respectively. The plots show close control of S about its target value and a steady-state i_{uc} of approximately 0. In the i_{uc} plot, positive values signify ultra-capacitor discharge, and negative currents signify charging the ultra-capacitor. Plot (h) shows the power delivered by both the fuel cell and the ultra-capacitor.

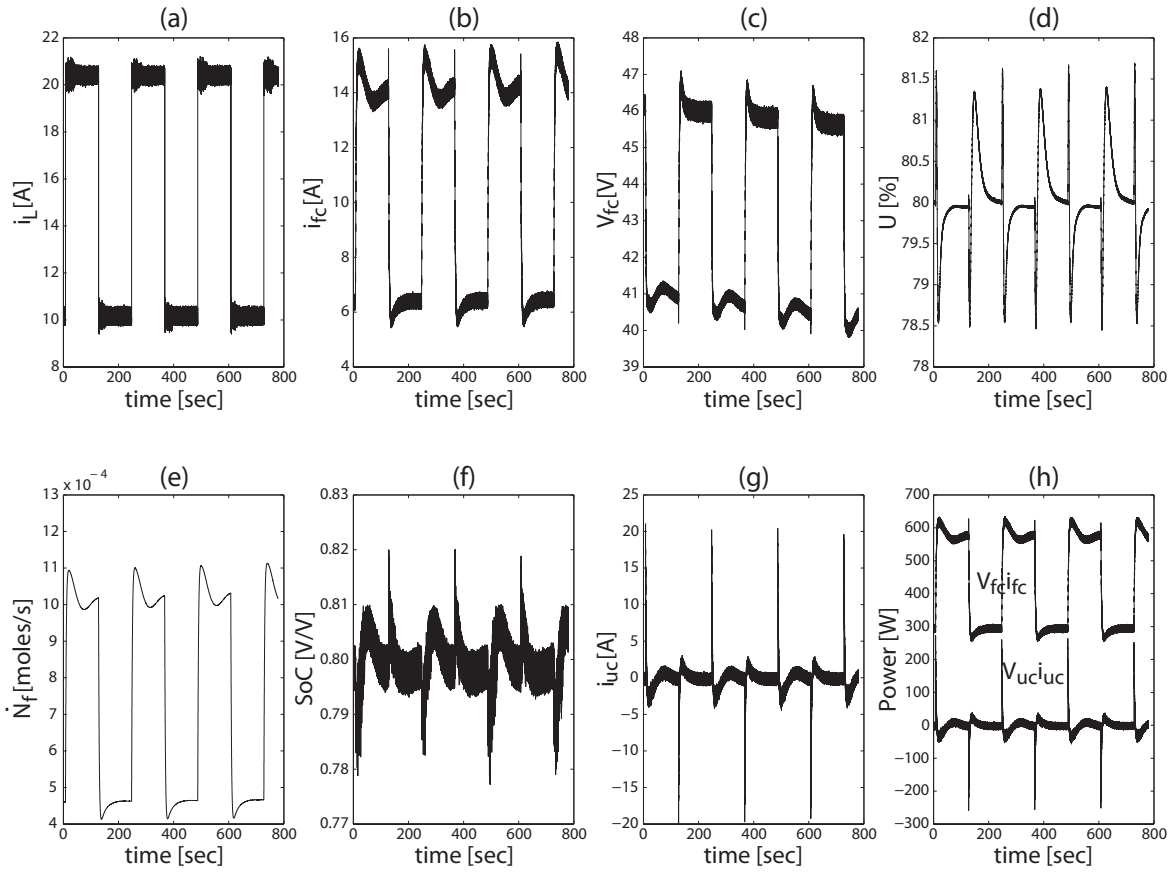

Figure 5.2: Adaptive Control under Step Changes in i_L

Figure 5.3 shows the efficiency estimates in solid lines and their initial values in dashed lines. Notice the recurring pattern in $\bar{\eta}_1$ in plot (a). Plots (b) and (c) show $\bar{\eta}_2$ and $\bar{\eta}_{12}$ steadily grow and decline, respectively. As mentioned previously in Section 4.2, these parameters will not necessarily converge, but will maintain a specific relationship, $(V_L i_L e_2 - V_{fc} i_{fc} e_{12}) \to 0$ as $t \to \infty$. In plot (b), $\bar{\eta}_2$ can be seen to saturate at 1. This portion of the plot is magnified in Figure 5.4. The saturation limits prevent the efficiency estimates from growing unbounded. Analytically, the system would still be stable under such conditions; however, this could result in practical and computational difficulties. We will see in the next test that the saturation of the parameter estimates does not adversely affect system performance.

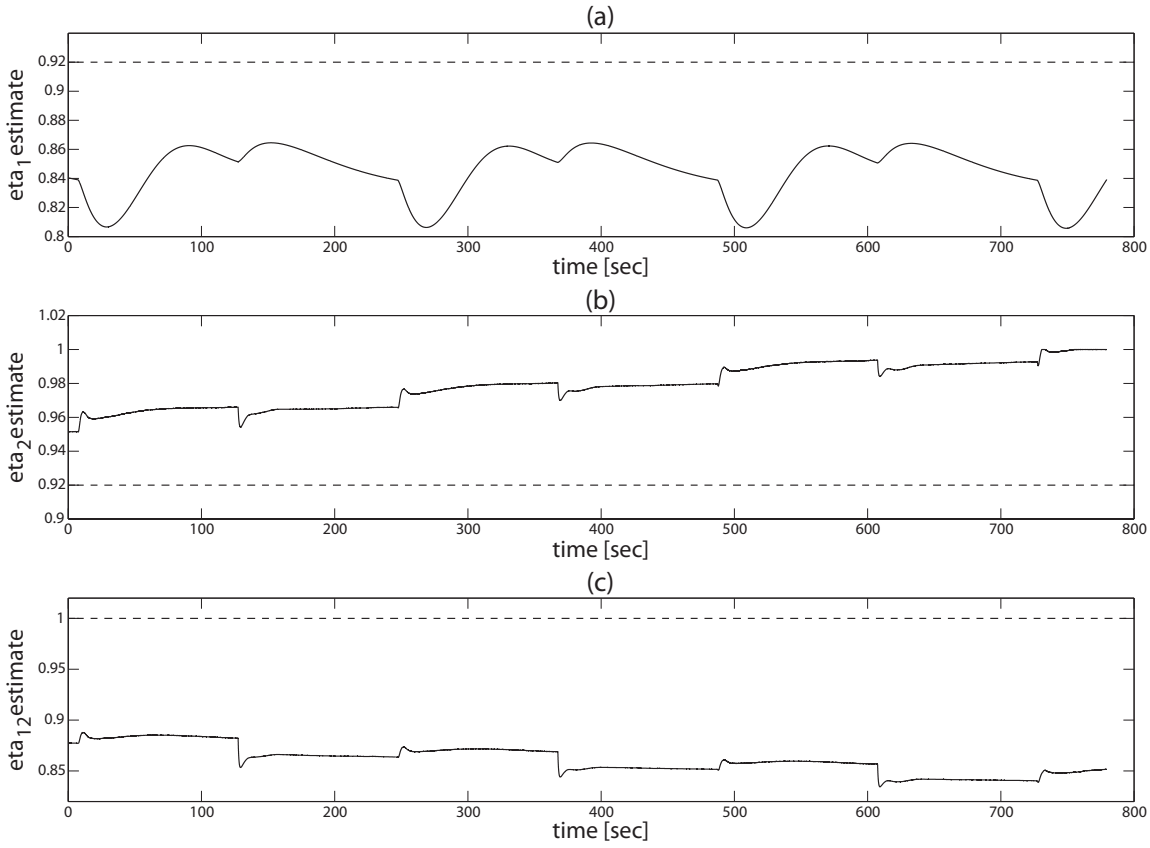

Figure 5.3: Adaptive Control Efficiency Estimates

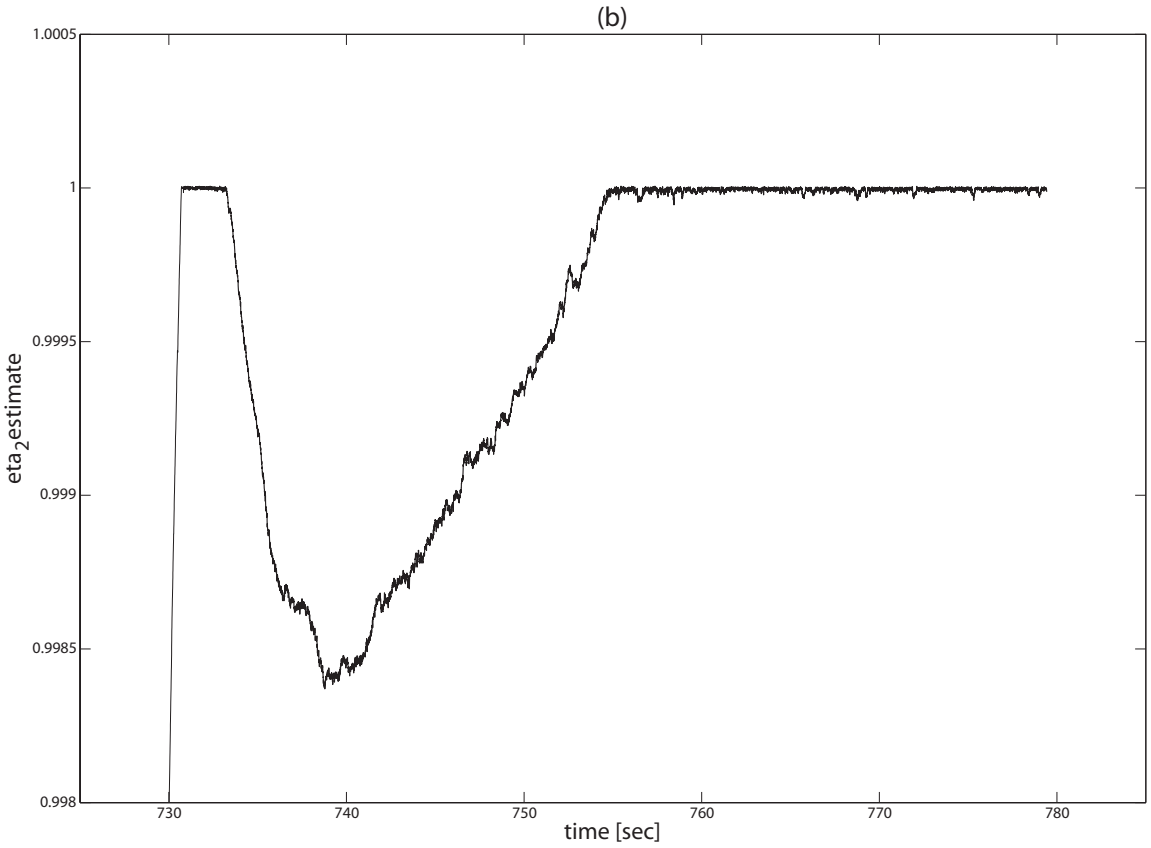

Figure 5.4: Adaptive Control Saturation in $\bar{\eta}_2$

Next, we compare the results with those from a FSS with a steady-state offset. The FSS was modeled as

$$\frac{\dot{N}_f(s)}{\dot{N}_{f,d}(s)} = \frac{0.85}{2s+1},$$

but, once again, this was assumed unknown during control development. The FSS again satisfies Equation (2.10) with the same β comparison function and with γ equal to 0.85 of its previous value. Therefore, Theorem 1 and Theorem 3 can be applied and the proposed control strategy therein is used. Except the FSS transfer function, all other system parameters and gains are the same as in the last experiment. These results are plotted in Figure 5.5. Plot (a) shows the same load profile that was used in the previous experiment. Plot (b) shows both the actual fuel cell current, i_{fc} and the demanded current, $i_{fc,d}$. Notice that i_{fc} follows $i_{fc,d}$ with an offset. This is due to the FSS dynamics assumed for this experiment. Transient i_{fc} is also shaped by current regulation, Equation (2.9). During the transience, the ultra-capacitor meets the deficit between the load requirement and what the fuel cell can provide. This can be seen in plot (g) and plot (h). Plot (d) and plot (f) show the utilization and SoC, respectively. Each is maintained close to its target value despite the changes in power demand. The ultimate bound on E_s was estimated using Equation (3.44) to be $\delta_{max} \approx 0.003$, which agrees with the steady-state fluctuations seen in plot (f). Measurement noise also contributes to the fluctuations in S.

Figure 5.6 contains a comparison of the results with and without an offset in the FSS. Plots (a1), (b1), (c1), and (d1) give results with the bounded tracking error, and plots (a2), (b2), (c2), and (d2) give results with zero steady-state tracking error. The controller performance, as evident from the transient control of U and control of S, shown in plots (c) and (d), is very similar between the two cases. Conversely, development of $i_{fc,d}$ and $\bar{\eta}_1$, shown in plots (a) and (b), are considerably different. The presence of the FSS tracking error causes a much higher $i_{fc,d}$, primarily due to the lower $\bar{\eta}_1$ estimate. The performance specification documents for the unidirectional DC/DC converter indicate 80-90% efficiency over the operating voltages of this test,

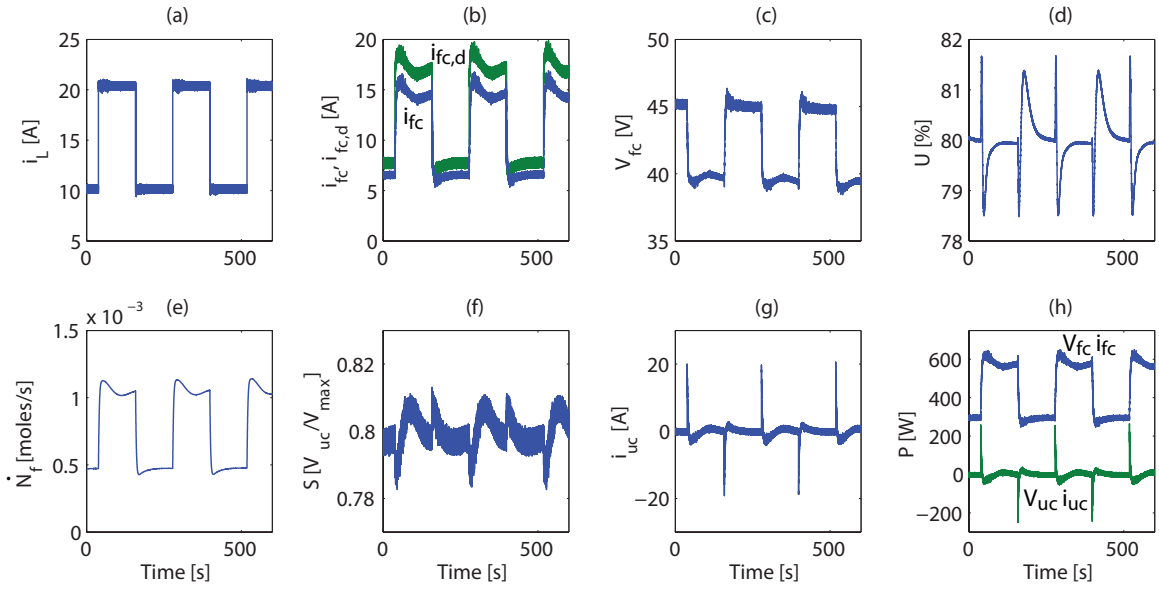

Figure 5.5: Adaptive Control with 15% offset FSS

suggesting that the presence of the tracking error degraded the estimate of η_1.

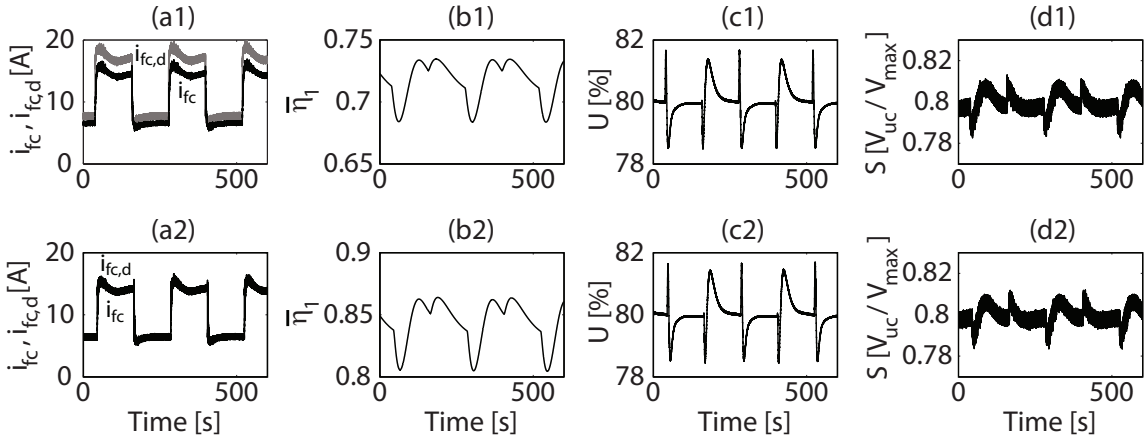

Figure 5.6: Controller Performance Comparison with Zero and Non-zero Steady-state FSS Tracking Error

5.3 Effect of Adaptation

In this section, we discuss the effects of adaptation in the current controller. For this comparison, the same FSS and controller are used with and without adaptation. Once again, the FSS is modeled as a first order system with no steady-state offset using

$$\frac{\dot{N}_f(s)}{\dot{N}_{f,d}(s)} = \frac{1}{2s+1}.$$

The adaptation gains have been set to zero $\gamma_1 = \gamma_2 = \gamma_{12} = 0$ for the case where there is no adaptation. All other system parameters are the same as the previous experiments unless otherwise noted.

Let us investigate controller performance as indicated by U. Figure 5.7 shows that the utilization converges toward the target value of 80% when adaptation is allowed. This was evident in the first data set as well, Figure 5.2. However, when there is no adaptation, there is an offset from the target value of approximately 3-4% at steady-state. Now that we have seen one of the effects of turning off the adaptation, let us

examine the cause and how to mitigate the deviation from the target value.

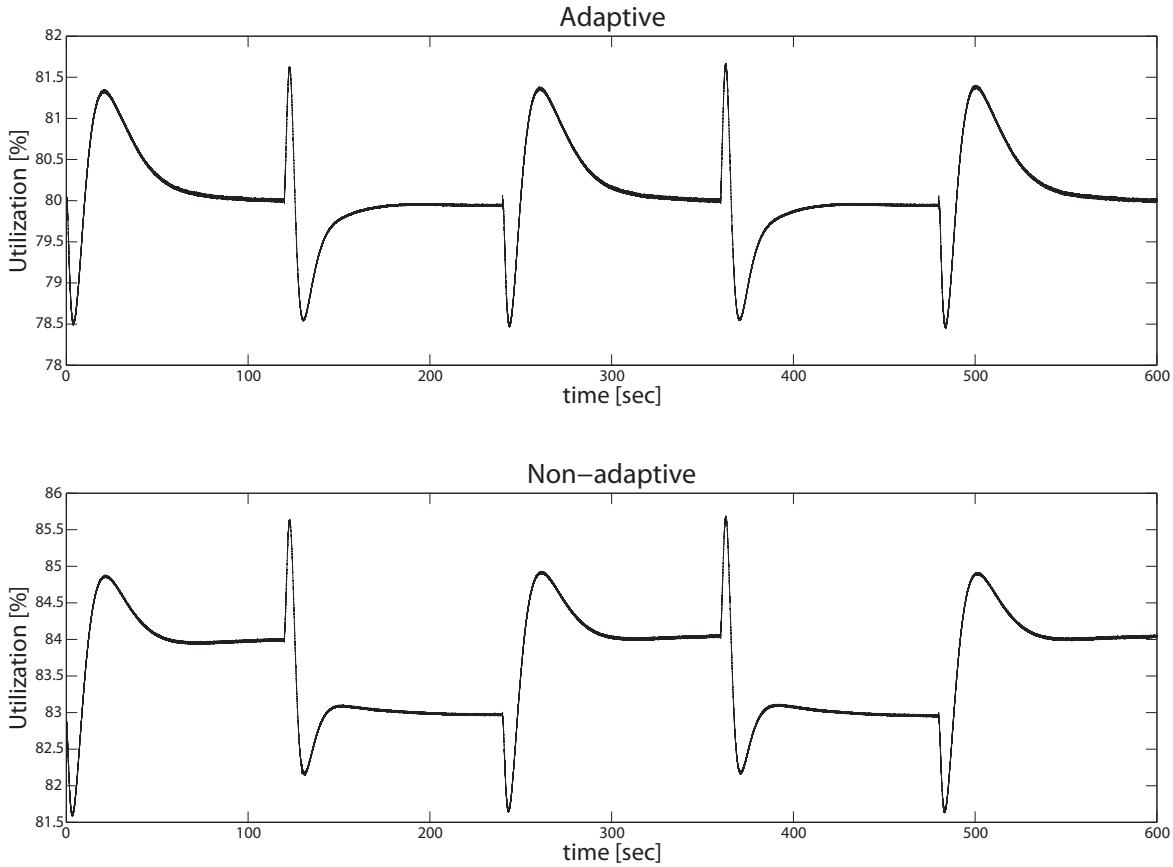

Figure 5.7: Comparison of U Between a Controller with Adaptation and One Without

From Equation (2.7), a steady-state utilization error, $E_{U_{ss}}$, can be expressed as

$$E_{U_{ss}} = U_{ss} - U_{ss,t} = \frac{4nF\dot{N}_f\mathcal{N}_{cell}(1-k)E_{fc}}{(4nF\dot{N}_f)^2 - 4nF\dot{N}_f(i_{fc}+i_{fc,t}) + (k\mathcal{N}_{cell})^2 i_{fc}i_{fc,t}}, \tag{5.1}$$

which is directly proportional to E_{fc}. If we examine the steady-state value of E_{fc} from its dynamical equation, Equation (3.31), we find that

$$E_{fc,ss} = \frac{V_L i_L e_2 - V_{fc} i_{fc} e_{12}}{k_p V_{uc} + \bar{\beta}_{12} V_{fc}}. \tag{5.2}$$

Without adaptation, $E_{fc,ss}$ is dependent on our initial estimates for β_2 and β_{12}. Without knowledge of the true values of η_1 and η_2, $E_{U_{ss}}$, and thus $E_{fc,ss}$, must be minimized

by increasing the design parameter k_p. For typical voltage values seen in these experiments, and considering a nominal value of $k_p = 0.2$, k_p must be increased almost twentyfold in order to reduce these errors by half. This is approximately the value of k_p that was used in the non-adaptive case shown in Figure 5.7. However, as k_p is increased, the amplitude of oscillations in i_{uc} grow, as seen in Figure 5.8. The frequency and amplitude of i_{uc} can grow too large for the DC/DC converters to handle, risking hardware damage. It is for this reason that the system was shut down at approximately 730 sec.

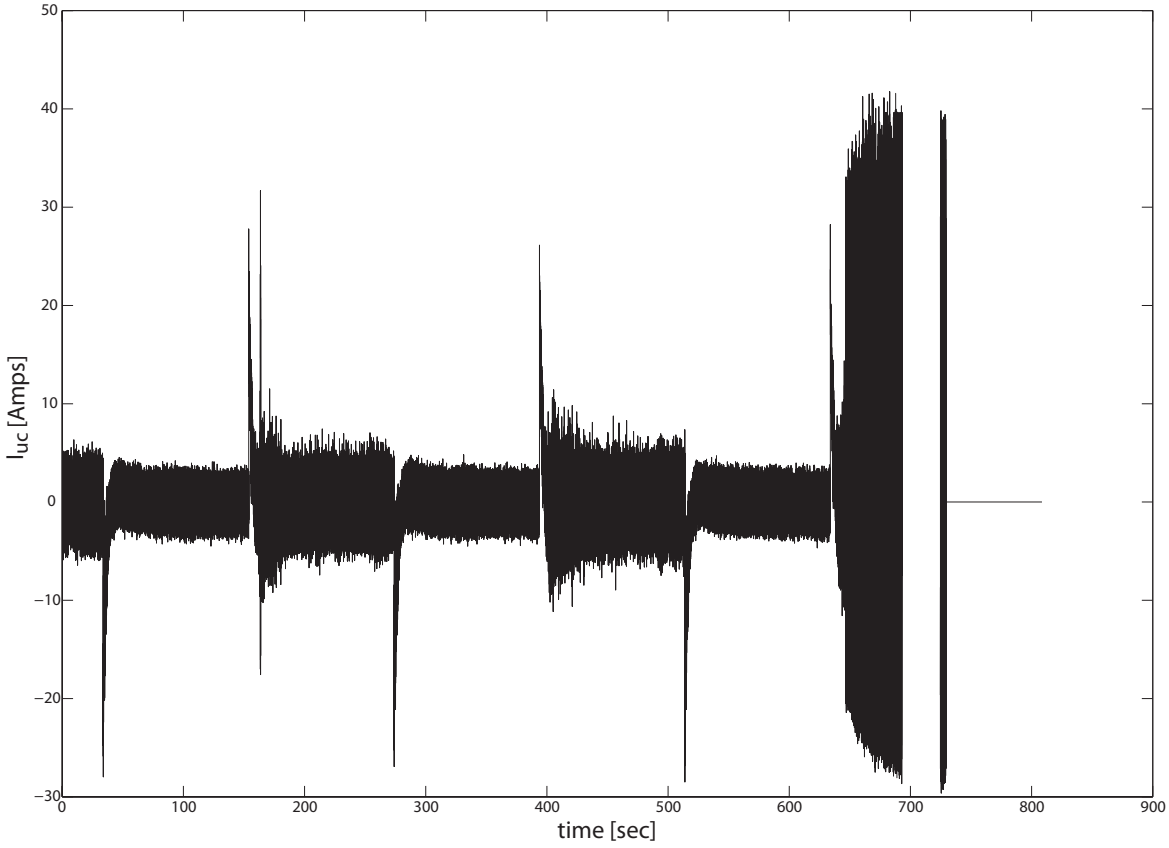

Figure 5.8: Ultra-capacitor Current Without Adaptation. System Shut Off at Approximately 730 sec.

Now, let us examine controller performance by examining S. As seen in Figure 5.9, the adaptive controller forces the state-of-charge toward its target value of 0.8,

but S drifts away from this target value in the non-adaptive case. Looking at the dynamical equation for E_s and setting $\dot{E}_s = 0$, we find that at steady-state,

$$E_{s,ss} = \frac{V_L i_L e_1 - V_{fc}(E_{fc} + E_{fc,t})}{k_s V_{fc}}. \tag{5.3}$$

As we can see in Equation (5.3), if E_{fc} and $E_{fc,t}$ are converging toward 0, E_s will still be non-zero for non-zero e_1. The value of $E_{s,ss}$ can be reduced by increasing k_s. However, as with k_p before, too large a value of k_s can lead to increased oscillations, this time in $i_{fc,d}$, which would result in constant changes in the fuel demand. This can lead to excessive wear of the FSS and potentially, system instability. The effect of an increased value for k_s was not tested due to the previous results of increasing k_p.

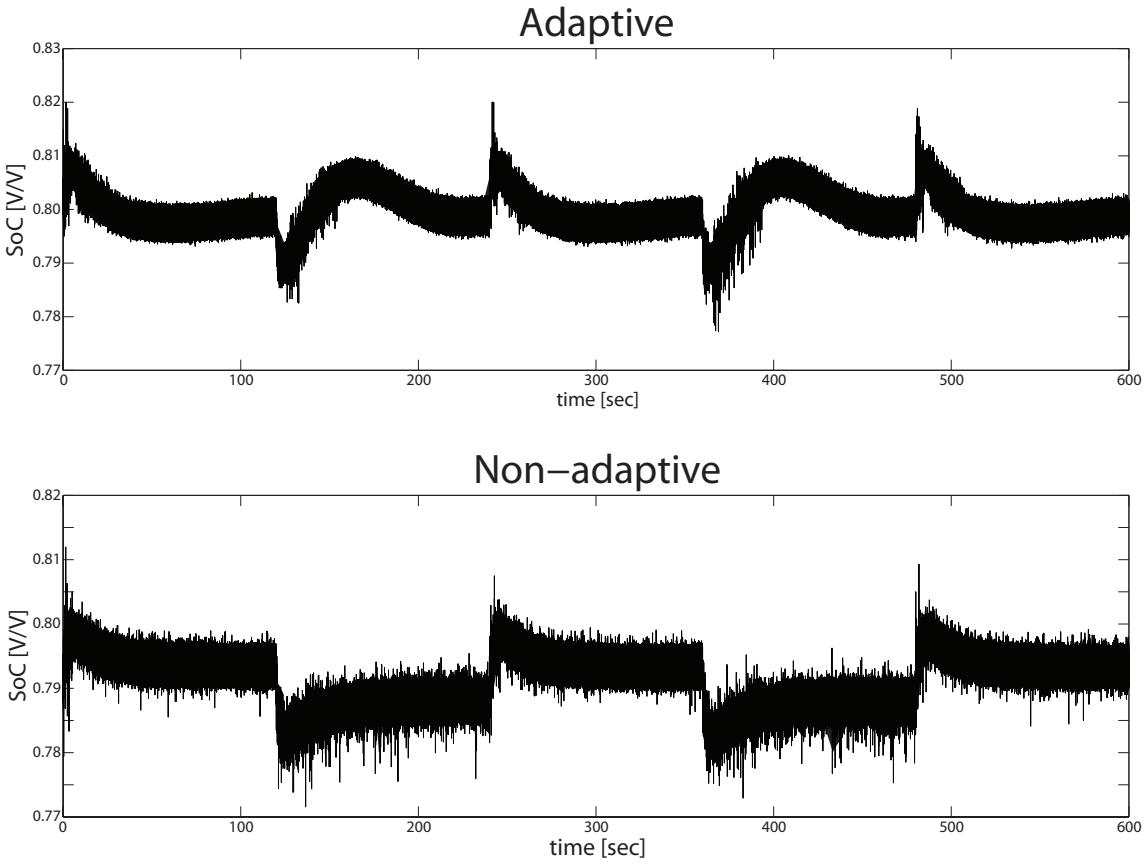

Figure 5.9: Comparison of S Between a Controller with Adaptation and One Without

Chapter 6

Conclusion

This thesis addresses the control of a hybrid SOFC ultra-capacitor system. Fuel starvation is addressed by controlling the fuel utilization, U. Using a steady-state property of the fuel cell, transient control of U is achieved by using a feedback-based current regulation method. The design of the controller herein assumes only a general stability behavior of the fuel supply system without precise knowledge of its dynamics. An ultra-capacitor is used to compensate for the deficit or excess power during transients.

An adaptive controller is developed to govern the system. The objectives addressed were to minimize the fluctuation in the fuel cell utilization during power demand transients, to maintain a target ultra-capacitor state-of-charge, and to meet the load requirements while ensuring robustness to uncertainties in the system. For the generalized FSS, the adaptive controller ensures that the SOC of the ultra-capacitor is bounded about the desired level in the presence of unknown DC/DC converter efficiencies that are treated as parameters. This same design admits asymptotic properties if the FSS displays exponentially decaying tracking error.

The control strategy developed was validated via simulation as well as hardware-in-the-loop experimentation. Simulation results suggest parameter convergence under a persistently exciting load profile. Experiments show that the controller is valid for fuel supply systems with outputs that track the desired value at an offset, as well as those with outputs that exponentially track the desired value.

The most immediate opportunity for future work, based on this thesis, is to develop analytical tools for predicting the onset of instability due to certain dynamic properties of the FSS. Possible techniques for this include absolute stability and the multi-variable circle criterion. Research on this topic is currently underway.

Another possible area for future work involves enhancing the current regulation method used in this work. Currently, this method only accounts for delays introduced by the fuel supply system dynamics, D_1. For better disturbance rejection, the regulation of i_{fc} should also account for delays introduced by the reformer, D_2. Further research is required to incorporate this delays using a model-independent or observer-based approach.

References

[1] J. Larminie and A. Dicks. *Fuel Cell Systems Explained*. John Wiley & Sons Ltd, Chichester, 2003.

[2] Jay T. Pukrushpan, Anna G. Stefanopoulou, and Huei. Peng. *Control Of Fuel Cell Power Systems*. Advances in industrial control. Springer, 2004.

[3] X. Li. *Principles of Fuel Cells*. Taylor and Francis Group, 2006.

[4] M. H. Nehrir and C. Wang. *Modeling and Control of Fuel Cells - Distributed Generation Applications*. John Wiley and Sons, Inc., 2009.

[5] T. Das and R. Weisman. A feedback based load shaping strategy for fuel utilization control in sofc systems. In *American Control Conference, 2009. ACC '09.*, pages 2767 –2772, 10-12 2009.

[6] J. R. Meacham, F. Jabbari, J. Brouwer, J. L. Mauzey, and G. S. Samuelsen. Analysis of stationary fuel cell dynamic ramping capabilities and ultra capacitor energy storage using high resolution demand data. *Journal of Power Sources*, 156(2):472 – 479, 2006.

[7] A. Lazzaretto, A. Toffolo, and F. Zanon. Parameter setting for a tubular sofc simulation model. *Journal of Energy Resources Technology*, 126(1):40–46, 2004.

[8] K. Sedghisigarchi and A. Feliachi. Control of grid-connected fuel cell power plant for transient stability enhancement. In *Power Engineering Society Winter Meeting, 2002. IEEE*, volume 1, pages 383 – 388 vol.1, 2002.

[9] S. Campanari. Thermodynamic model and parametric analysis of a tubular sofc module. *Journal of Power Sources*, 92(1-2):26 – 34, 2001.

[10] K. Rajashekara, J. A. MacBain, and M. J. Grieve. Evaluation of SOFC hybrid systems for automotive propulsion applications. *IEEE Industry Applications Conference*, pages 1593–1597, 2006.

[11] P. Aguiar, D. J. L. Brett, and N. P. Brandon. Feasibility study and techno-economic analysis of an SOFC/battery hybrid system for vehicle applications. *Journal of Power Sources*, 171:186–197, 2007.

[12] R. Bove and S. Ubertini. *Modeling Solid Oxide Fuel Cells: Methods, Procedures, and Techniques*. Fuel Cells and Hydrogen Energy. Springer, 2008.

[13] A.J. Slippey. Dynamic modeling and analysis of multiple sofc system configurations. Master's thesis, Rochester Institute of Technology, 2009.

[14] F. Mueller, J. Brouwer, F. Jabbari, and S. Samuelsen. Dynamic simulation of an integrated solid oxide fuel cell system including current-based fuel flow control. *Journal of Fuel Cell Science and Technology*, 3(2):144–154, 2006.

[15] F. Bidault, D.J.L. Brett, P.H. Middleton, and N.P. Brandon. Review of gas diffusion cathodes for alkaline fuel cells. *Journal of Power Sources*, 187(1):39 – 48, 2009.

[16] Betty Y.S. Lin, Donald W. Kirk, and Steven J. Thorpe. Performance of alkaline fuel cells: A possible future energy system? *Journal of Power Sources*, 161(1):474 – 483, 2006.

[17] Aiguo Liu and Yiwu Weng. Performance analysis of a pressurized molten carbonate fuel cell/micro-gas turbine hybrid system. *Journal of Power Sources*, 195(1):204 – 213, 2010.

[18] P.M. Biesheuvel and J.J.C. Geerlings. Thermodynamic analysis of direct internal reforming of methane and butane in proton and oxygen conducting fuel cells. *Journal of Power Sources*, 185(2):1162 – 1167, 2008.

[19] N. Sammes, R. Bove, and K. Stahl. Phosphoric acid fuel cells: Fundamentals and applications. *Current Opinion in Solid State and Materials Science*, 8(5):372 – 378, 2004.

[20] C. Wang and A.J. Appleby. High-peak-power polymer electrolyte membrane fuel cells. *Journal of The Electrochemical Society*, 150(4):A493–A498, 2003.

[21] J. J. Baschuk and X. Li. Modelling of polymer electrolyte membrane fuel cells with variable degrees of water flooding. *Journal of Power Sources*, 86(1-2):181 – 196, 2000.

[22] E. Jannelli, M. Minutillo, and E. Galloni. Performance of a polymer electrolyte membrane fuel cell system fueled with hydrogen generated by a fuel processor. *Journal of Fuel Cell Science and Technology*, 4(4):435–440, 2007.

[23] A. Drolia, P. Jose, and N. Mohan. An approach to connect ultracapacitor to fuel cell powered electric vehicle and emulating fuel cell electrical characteristics using switched mode converter. In *Industrial Electronics Society, 2003. IECON '03. The 29th Annual Conference of the IEEE*, volume 1, pages 897 – 901 vol.1, 2-6 2003.

[24] P. Thounthong, S. Ral, and B. Davat. Control strategy of fuel cell/supercapacitors hybrid power sources for electric vehicle. *Journal of Power Sources*, 158(1):806 – 814, 2006.

[25] A. Vahidi, A. Stefanopoulou, and H. Peng. Current management in a hybrid fuel cell power system: A model-predictive control approach. *Control Systems Technology, IEEE Transactions on*, 14(6):1047 –1057, nov. 2006.

[26] W. Schmittinger and A. Vahidi. A review of the main parameters influencing long-term performance and durability of pem fuel cells. *Journal of Power Sources*, 180(1):1 – 14, 2008.

[27] J. Sun and I.V. Kolmanovsky. Load governor for fuel cell oxygen starvation protection: A robust nonlinear reference governor approach. *Control Systems Technology, IEEE Transactions on*, 13(6):911 – 920, nov. 2005.

[28] A. Arce, A. J. del Real, and C. Bordons. Mpc for battery/fuel cell hybrid vehicles including fuel cell dynamics and battery performance improvement. *Journal of Process Control*, 19(8):1289 – 1304, 2009.

[29] M. Uzunoglu and M.S. Alam. Dynamic modeling, design and simulation of a pem fuel cell/ultra-capacitor hybrid system for vehicular applications. *Energy Conversion and Management*, 48(5):1544 – 1553, 2007.

[30] V. Paladini, T. Donateo, A. de Risi, and D. Laforgia. Super-capacitors fuel-cell hybrid electric vehicle optimization and control strategy development. *Energy Conversion and Management*, 48(11):3001 – 3008, 2007.

[31] A. Hajizadeh and M. Golkar. Intelligent power management strategy of hybrid distributed generation system. *International Journal of Electrical Power & Energy Systems*, 29(10):783 – 795, 2007.

[32] Z. Jiang, L. Gao, and R. A. Dougal. Adaptive control strategy for active power sharing in hybrid fuel cell/ battery power sources. *IEEE Transactions on Energy Conversion*, 22(2):507–515, 2007.

[33] E.M. Fleming and I.A. Hiskens. Dynamics of a microgrid supplied by solid oxide fuel cells. In *Bulk Power System Dynamics and Control - VII. Revitalizing Operational Reliability, 2007 iREP Symposium*, pages 1 –10, Aug. 2007.

[34] M.Y. Ayad, M. Becherif, A. Djerdir, and A. Miraoui. Sliding mode control for energy management of dc hybrid power sources using fuel cell, batteries and supercapacitors. In *Clean Electrical Power, 2007. ICCEP '07. International Conference on*, pages 500 –505, 21-23 2007.

[35] P. Rodatz, G. Paganelli, A. Sciarretta, and L. Guzzella. Optimal power management of an experimental fuel cell/supercapacitor-powered hybrid vehicle. *Control Engineering Practice*, 13(1):41 – 53, 2005.

[36] Michel Fliess, Jean Lvine, and Pierre Rouchon. Flatness and defect of nonlinear systems: Introductory theory and examples. *International Journal of Control*, 61:1327–1361, 1995.

[37] A. Payman, S. Pierfederici, and F. Meibody-Tabar. Energy control of supercapacitor/fuel cell hybrid power source. *Energy Conversion and Management*, 49(6):1637 – 1644, 2008.

[38] T. Allag and T. Das. Robust control of solid oxide fuel cell ultracapacitor hybrid system. *Control Systems Technology, IEEE Transactions on*, PP(99):1 –10, 2011.

[39] R. Kandepu, L. Imsland, B. A. Foss, C. Stiller, B. Thorud, and O. Bolland. Modeling and control of a SOFC-GT-based autonomous power system. *Energy*, 32:406–417, 2007.

[40] T. Das, S. Narayanan, and R. Mukherjee. Steady-state and transient analysis of a steam-reformer based solid oxide fuel cell system. *ASME Journal of Fuel Cell Science and Technology*, 7(1), 2010.

[41] H. K. Khalil. *Nonlinear Systems*. Prentice Hall, Upper Saddle River, NJ, third edition edition, 2002.

[42] C. Meyer. *Matrix Analysis and Applied Linear Algebra*. Society for Industrial and Applied Mathematics, 2000.

[43] T. Allag. Robust control strategies for hybrid solid oxide fuel cell systems. Master's thesis, Rochester Institute of Technology, 2010.